nature communications

Article

https://doi.org/10.1038/s41467-025-68024-5

Intranasal blood-brain barrier bypass enables sequential mitochondria-targeted bioengineered nanolamellar system for ischemic stroke therapy

Received: 6 June 2025

Accepted: 15 December 2025

Published online: 17 January 2026

Check for updates

Yue Yin[1,2], Zixuan Li[1,2], Weijie Shu[1,2], Hening Liu[1,2], Zihan Wang[1,2], Cong Fu[1,2], Yuanbo Zhu[1,2], Xuejing Li[1,2], Yi Zhang[1,2], Bei Lv[1,2], Zixuan Wang[1,2], Qiaoqiao Zhao[1,2], Dan Liu[3] ✉, Lu Tang[4] ✉ & Wei Wang[1,2] ✉

Mitochondrial damage constitutes the central pathological mechanism of cerebral ischemia-reperfusion (I/R) injury. Targeted delivery of antioxidants to mitochondria and the phenotype polarization of glial cells holds great promise for effective treatment. However, the blood-brain barrier (BBB) remains a major obstacle, causing insufficient drug accumulation in neuronal mitochondria. Here, we develop a bioengineered nanolamellar system (MM@BPPF) by coating microglia-mitochondria hybrid biomembrane onto black phosphorus nanosheets (BP NSs) loaded with polymetformin (PolyMet) and fingolimod hydrochloride (FTY720). Microglia membrane facilitates inflammation-directed targeting to the injured brain regions, while mitochondria membrane confers homotypic targeting to mitochondria. Meanwhile, BP NSs, PolyMet, and FTY720 act sequentially to restore mitochondrial function of neuronal cells and modulate microglial polarization. Intranasal administration enables MM@BPPF to bypass the BBB, substantially improving brain-targeting efficiency. This work not only offers an innovative sequential targeting strategy for mitigating I/R injury but also presents a potential paradigm for treating other central nervous system disorders.

Ischemic stroke (IS), a cerebrovascular disease triggered by stenosis or occlusion of cerebral blood vessels, is the second leading cause of adult mortality worldwide[1–3]. Although current treatment strategies, including thrombolytic therapy, mechanical thrombectomy, and neuroprotection, can partially alleviate symptoms, these therapeutic methods often fail to fully restore neurological function and may lead to ischemia-reperfusion (I/R) injury[4–6]. Oxidative stress and inflammatory storms are the primary contributors to I/R injury, with mitochondrial damage in neurons constituting the central pathological mechanism. As the core source of neuronal energy, mitochondria are highly susceptible to hypoxia and reoxygenation, which disrupts the mitochondrial respiratory chain, leading to electron leakage and excessive production of mitochondrial reactive oxygen species (mtROS). The accumulation of mtROS directly impairs mitochondrial function, leading to reduced adenosine triphosphate (ATP) production, disrupted calcium homeostasis, and accelerated neuronal apoptosis and necrosis[7]. Moreover, damaged mitochondria release various damage-associated components such as mitochondrial DNA (mtDNA),

[1]State Key Laboratory of Natural Medicines, Department of Pharmaceutics, School of Pharmacy, China Pharmaceutical University, Nanjing, P. R. China. [2]NMPA Key Laboratory for Research and Evaluation of Cosmetics, China Pharmaceutical University, Nanjing, P. R. China. [3]German Center for Neurodegenerative Diseases (DZNE), Bonn, Germany. [4]Institute for Experimental Molecular Imaging, Uniklinik RWTH Aachen and Helmholtz Institute for Biomedical Engineering, RWTH Aachen University, Aachen, Germany. ✉e-mail: dan.liu@dzne.de; ltang@ukaachen.de; wangcpu209@cpu.edu.cn

which trigger a potent inflammatory response and further exacerbate neuronal death[8]. Beyond direct neuronal damage, the excessive generation of mtROS and inflammatory mediators during I/R injury induces the transition of microglia into the pro-inflammatory M1 phenotype[9]. As the resident immune cells of the central nervous system (CNS), microglia undergo dynamic phenotypic transitions following IS[10]. Specifically, M1 microglia secrete pro-inflammatory cytokines that aggravate brain injury and impede functional recovery, whereas M2 microglia exert neuroprotective and reparative functions[11]. Given the spatiotemporal complexity of this pathological progression, the on-demand administration of antioxidants and glial polarization modulators is proposed to achieve optimal therapeutic efficacy. However, pervious studies have indicated that the simultaneous delivery of antioxidants and anti-inflammatory agents results in poor efficacy because these therapeutics are intended to work at different stages of ischemic injury[12]. Therefore, developing innovative drug delivery platforms capable of targeting mitochondria and modulating microglial polarization in a sequential mode represents a promising therapeutic strategy for ischemic stroke treatment.

Black phosphorus nanosheets (BP NSs), a novel two-dimensional nanomaterial composed of wrinkled honeycomb layers of phosphorus (P) atoms, have garnered significant attention across various fields due to their exceptional reactive oxygen species (ROS)-scavenging capability, anti-inflammatory property, and ability to regulate mitochondrial morphology and functions[13–15]. Notably, the layer-packed structure of BP NSs facilitates rapid electron transfer, while their elemental composition enables fast oxidative interactions, culminating the formation of P-O bonds. This unique mechanism allows BP NSs to efficiently scavenge excess ROS, highlighting their potential as effective antioxidants[16–18]. Upon chemical interaction with ROS, BP NSs degrade into non-toxic phosphorus oxides, underscoring their superior biocompatibility. More importantly, phosphate ions (PO_4^{3-}), a degradation product of BP NSs, play a crucial role in biomineralization and can react with intracellular calcium to mitigate calcium overload caused by mitochondrial dysfunction[19]. Furthermore, the negative charge and corrugated surface structure of BP NSs render them highly suitable as drug delivery vehicles[20]. Collectively, these properties position BP NSs as a promising nanoplatform for modulating multiple pathological hallmarks of IS and restoring mitochondrial function. AMP-activated protein kinase (AMPK) is a key endogenous defensive molecule that plays a pivotal role in the response to harmful stimuli during cerebral IS. Activation of AMPK promotes the secretion of anti-inflammatory cytokines and facilitates the reprogramming of microglia from pro-inflammatory M1 phenotype to neuroprotective M2 phenotype[21]. Metformin, a well-known AMPK activator widely used in the treatment of type 2 diabetes, has been reported to reduce infarct volume and alleviate neurological deficits by inhibiting neuronal apoptosis, promoting mitochondrial biogenesis, and stimulating angiogenesis after stroke attack[22]. In our previous work, we synthesized a cationic polymer, polymetformin (PolyMet), which inherits the therapeutic properties of metformin by covalently linking chitosan with dicyandiamide through an addition reaction[23–25]. Thus, we aimed to further investigate whether the combination of PolyMet and BP NSs could exert synergistic therapeutic effects in IS treatment. Additionally, fingolimod hydrochloride (FTY720), an anti-inflammatory agonist of the sphingosine 1-phosphate receptor (S1PR), has been reported to promote microglial polarization from the M1 phenotype to the M2 phenotype, suggesting its potential neuroprotective effects in IS[26]. Moreover, FTY720 is reported to elevate ATP levels, maintain calcium homeostasis, regulate mitophagy, facilitate mitochondrial biogenesis, and restore normal mitochondrial morphology and function through S1P-S1PRs axis and the activation of the signal transducer and activator of transcription 3 (STAT3)[27,28]. Building on these findings, we further explored the therapeutic potential of FTY720 in IS treatment.

Nevertheless, the BBB poses a significant challenge by impeding drug penetration into the brain parenchyma, thereby constraining the therapeutic efficacy of cerebral IS treatments[29–31]. In recent years, intranasal administration has emerged as a promising alternative option for CNS disease treatment[32–34]. Following intranasal delivery, bioactive agents can be absorbed through the nasal mucosa and transported directly to the brain via the olfactory and trigeminal nerve pathways[20]. Compared to gastrointestinal delivery and intravenous administration, intranasal delivery effectively bypasses the BBB, avoids first-pass metabolism and gastrointestinal exposure, thus serving as a preferred route for intracerebral drug delivery[35,36]. Additionally, bioengineered strategies have been increasingly employed to camouflage nanoparticles (NPs), imparting them with unique physicochemical and biological properties, such as enhanced biocompatibility, prolonged systemic circulation time, and innate targeting capabilities[37–40]. For instance, cloaking NPs with microglia membrane (MicM) facilitates preferential recruitment to cerebral infarct regions due to the strong affinity between microglia and the inflamed endothelial cells of the ischemic brain[41,42]. Meanwhile, membrane derived from subcellular organelles (e.g., mitochondria, endoplasmic reticulum) retains specific homotypic targeting proteins, enabling precise subcellular localization and modulation[43]. Therefore, fusing MicM with mitochondria membrane (MitM) to create a hybrid biomembrane coating represents a promising strategy for achieving sequential targeting. By virtue of this design, the bioinspired nanoplatform can first selectively accumulate in cerebral infarct regions and subsequently localize within damaged neuronal mitochondria, thereby enhancing therapeutic precision and efficacy.

On this basis, our work reported a bioengineered nanolamellar system (MM@BPPF) designed to ameliorate I/R injury by sequentially targeting IS lesions and neuronal mitochondria, while modulating neuroinflammation through the microglial phenotypic transition from M1 to M2 state. To be more specific, this bioengineered nanolamellar system was constructed using hybrid nanovesicles composed of MitM and MicM, which further encapsulated BP NSs loaded with the AMPK activator PolyMet and the microglia regulator FTY720 (Fig. 1A). The combination of FTY720 and PolyMet with BP NSs facilitated the co-delivery of antioxidants and glial polarization agents, establishing a sequential therapeutic strategy mediated by the rapid ROS responsiveness of BP NSs and the distinct intracellular targets of the loaded agents. BP NSs functioned as potent antioxidants while simultaneously exerting anti-inflammatory, calcium-regulating, and angiogenesis-promoting effects. PolyMet and FTY720 exhibited synergistic anti-stroke mechanisms via modulating microglial phenotype and alleviating neuroinflammation. By incorporating a hybrid biomembrane coating, BP-based nanolamellar system acquired biomimetic properties that facilitated the co-targeting of neuronal mitochondria through multiple “self-marker” proteins expressed on both MitM and MicM. In vitro studies demonstrated that MM@BPPF effectively traversed the olfactory epithelium, penetrated the deep layers of H_2O_2-exposed neuronal spheroids, and co-localized within the mitochondria of damaged neurons. Consequently, MM@BPPF efficiently scavenged excessive mtROS, alleviated calcium overload, restored energy supply, and ultimately rescued neurons by restoring mitochondrial function. Following intranasal administration, MM@BPPF bypassed the BBB, avoided systemic adverse effects, and selectively accumulated in the mitochondria of neurons within ischemic brain regions. As a result, infarct volume, brain edema, and neuronal apoptosis were significantly attenuated in middle cerebral artery occlusion/reperfusion (MCAO/R) rats, accompanied with improved neuronal regeneration and recovered cognitive function. Further investigations revealed that the therapeutic effects of MM@BPPF were mediated not only through scavenging excess ROS, restoring mitochondrial function, and suppressing neuroinflammation, but also by remodeling the ischemic microenvironment via microglial polarization and enhanced

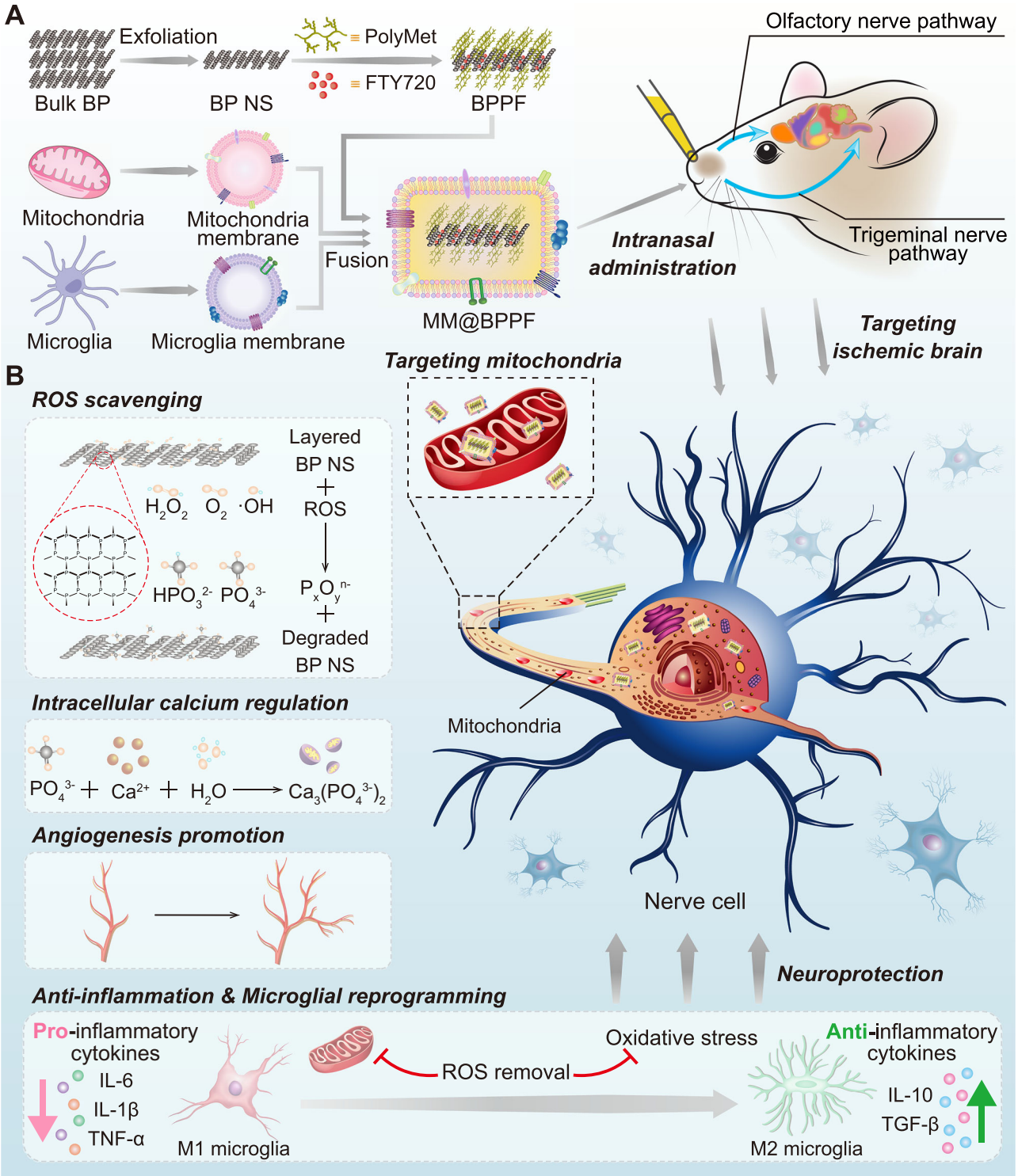

Fig. 1 | Schematic illustration of the study design. A Fabrication process of MM@BPPF. **B** Underlying neuroprotective mechanisms of MM@BPPF in IS therapy.

angiogenesis (Fig. 1B). Overall, this bioengineered nanolamellar system presents an innovative sequential mitochondrial targeting strategy for neuronal repair following IS and holds significant therapeutic potential for treating other CNS disorders via coordinated neuroprotection and brain remodeling.

Results

Synthesis and characterization of MM@BPPF

In this work, MM@BPPF was prepared according to the scheme shown in Fig. 1A. Firstly, bulk BP was exfoliated into BP NSs using the liquid-phase exfoliation method as previously described[44,45]. Next, PolyMet and FTY720 were loaded onto BP NSs by electrostatic reaction to acquire BPPF. Subsequently, MitM and MicM were extracted and fused into a hybrid membrane (MM) according to the reported protocol[46,47]. Finally, MM was repeatedly co-extruded with BPPF to functionalize the surface of BPPF, eventually forming the bioengineered nanolamellar system (MM@BPPF).

The morphologies of BP NSs were observed using transmission electron microscopy (TEM). As shown in their TEM image, BP NSs exhibited a two-dimensional nanosheet structure with a sharp edge

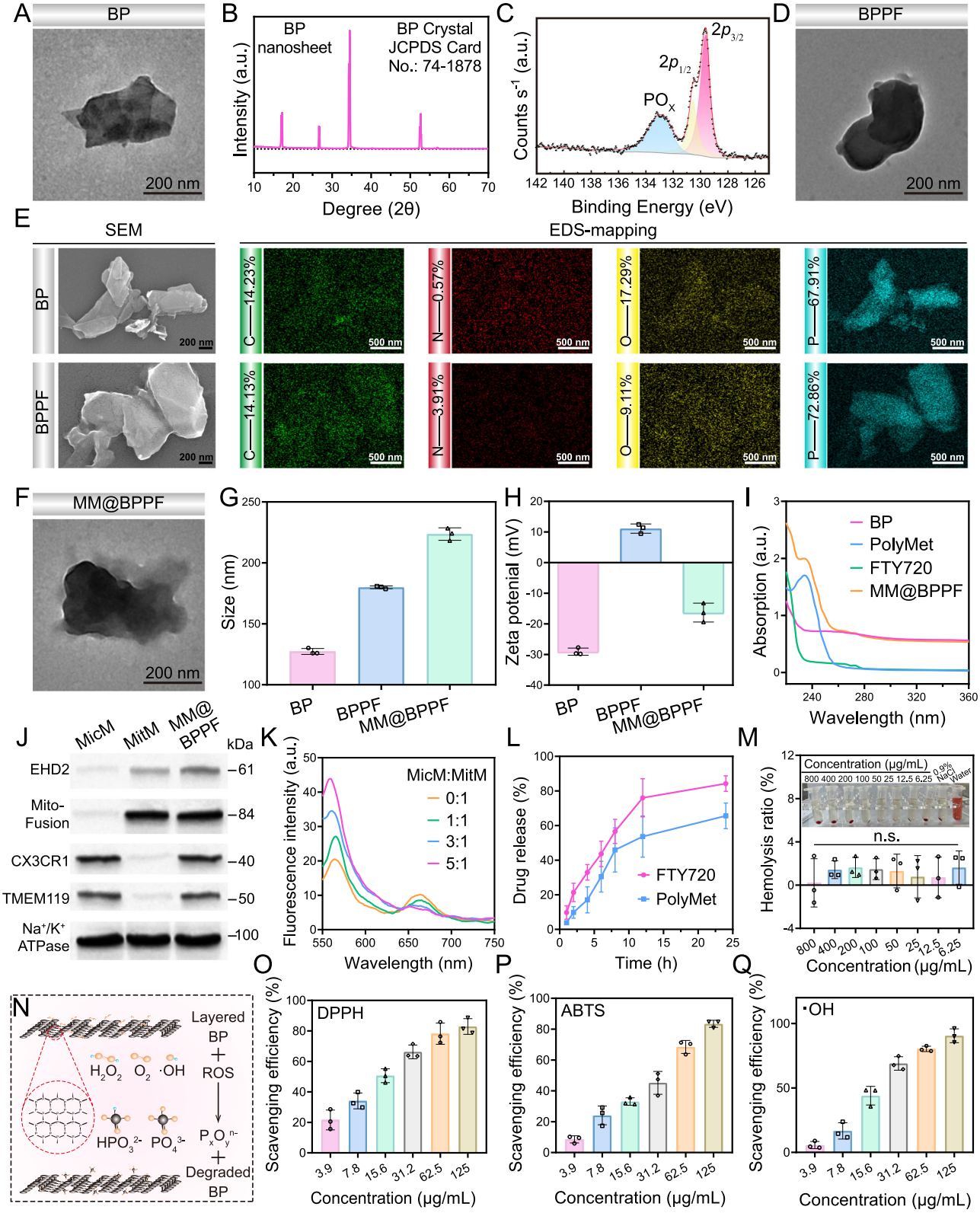

(Fig. 2A). In addition, X-ray diffraction (XRD) results revealed that the peaks of the prepared BP NSs were consistent with those of the standard BP crystal, with no evidence of new crystal lattice formation (Fig. 2B)[48]. Moreover, X-ray photoelectron spectroscopy (XPS) demonstrated the existence of characteristic peaks corresponding to P-P bond at 129.63 eV and P-O bond at 132.93 eV in BP NSs (Fig. 2C). Taken together, these findings confirmed the successful preparation of BP NSs. To achieve synergistic pharmacological effects, both the cationic polymer PolyMet and the cationic anti-inflammatory agonist FTY720 were simultaneously physiosorbed onto the anionic BP NSs[49]. TEM images of BPPF showed that its lamellar structure was less clear compared to naked BP NSs, indicating the interaction between PolyMet, FTY720, and BP NSs (Fig. 2D). Scanning electron microscopy (SEM) images and elemental mapping in Fig. 2E further evidenced an increase in nitrogen content from 0.57% in BP NSs to 3.91% in BPPF, validating the successful integration of both therapeutic agents onto BP NSs.

Fig. 2 | Synthesis and characterization of MM@BPPF. A TEM image of BP NSs, scale bar: 200 nm. The TEM image was representative data from 3 independent experiments. **B** XRD spectrum, and **C** XPS spectrum of BP NSs. **D** TEM image of BPPF, scale bar: 200 nm. The TEM image was representative data from 3 independent experiments. **E** SEM image and elemental mapping of BP NSs and BPPF. The SEM images and elemental mapping images were representative data from 3 independent experiments. **F** TEM image of MM@BPPF, scale bar: 200 nm. The TEM image was representative data from 3 independent experiments. **G** Hydrodynamic diameters, and **H** zeta potentials of BP NSs, BPPF, and MM@BPPF. **I** UV–vis spectra of BP NSs, FTY720, PolyMet, and MM@BPPF. **J** Western blotting assay of MicM, MitM, and MM@BPPF. The immunoblots image was representative data from 3 independent experiments. **K** FRET assay of the fusion of MicM and MitM. **L** In vitro cumulative drug release manners of FTY720 and PolyMet from MM@BPPF at pH 6.7. **M** Hemolysis test of MM@BPPF in different concentrations. **N** Schematic illustration of the ROS scavenging mechanism of BP NSs. Quantitative analysis of **O** DPPH, **P** ABTS, and **Q** •OH scavenging ability of MM@BPPF. The data represent the means ± SD, $n = 3$ independent experiments in (**G**, **H**, **L**, **M**, **O**–**Q**). Statistics: one-way ANOVA with Tukey's multiple comparison test (**M**). Source data are provided as a Source Data file.

To impart ischemic tissue and mitochondrial targeting capabilities to the nanolamellar system, BPPF was further camouflaged with MM composed of MicM from BV2 cell and MitM from PC12 cells. The MitM and MicM were extracted and co-extruded with BPPF to fabricate the MM@BPPF. As the TEM images clearly revealed, the MM successfully adhered to the surface of the BPPF (Fig. 2F). The average hydrodynamic diameters of BP NSs, BPPF, and MM@BPPF were approximately 127, 180, and 224 nm in average, respectively (Fig. 2G and Supplementary Fig. 1). The stepwise increase in particle size following drug loading and cell membrane encapsulation confirmed the successful assembly process of MM@BPPF. Meanwhile, the observed variations in zeta potential measurements aligned with each modification step (Fig. 2H). Furthermore, UV–vis absorption of MM@BPPF presented typical absorption peaks of PolyMet at 234 nm (Fig. 2I)[50]. Moreover, the essential proteins on the MitM and MicM were characterized by western blotting assay. As shown in Fig. 2J, EHD2 and Mitofusion, the key proteins involved in mitochondrial targeting and penetration, were retained on MitM and MM@BPPF[43]. Chemokine C-X3-C motif receptor 1 (CX3CR1) and transmembrane protein 119 (TMEM119) were reported to be the crucial proteins of microglia responsible for signaling and recruitment. Importantly, TMEM119 is specifically expressed on microglia and plays a vital role in regulating microglial function. The presence of both CX3CR1 and TMEM119 on MicM and MM@BPPF implicated that the functional properties of MicM were preserved on the bioengineered nanoplatform[51,52]. Meanwhile, Förster resonance energy transfer (FRET) study was conducted to verify the membrane fusion process. MicM was added into DiD- and DiI-labeled MitM in an increased ratio. DiI and DiD were respectively served as fluorescence donor and acceptor, when they are in close distance, the fluorescence energy will transfer from donor to acceptor. As the weight ratio of MicM to MitM increased, fluorescence intensity at 565 nm gradually increased, while the fluorescence at 663 nm correspondingly declined, demonstrating the successful membrane fusion between MitM and MicM (Fig. 2K)[46]. The release profiles of FTY720 and PolyMet were assessed using UV–vis spectroscopy in environments simulating cerebral ischemic regions (pH 6.7) and normal physiological environment (pH 7.4). The results revealed that around 84% of FTY720 and 66% of PolyMet were released at pH 6.7, demonstrating efficient drug release behaviors under ischemic lesion-mimicking conditions (Fig. 2L). Conversely, under normal physiological conditions, FTY720 and PolyMet displayed minimal cumulative release rates, with only 18.94 ± 2.69% and 16.49 ± 0.97%, respectively (Supplementary Fig. 2). Hydrodynamic diameter and polydispersity index (PDI) measurements indicated that no obvious changes were observed within 144 h (Supplementary Fig. 3). These results demonstrated the pH-responsive property of MM@BPPF alongside its stability under physiological environment. Furthermore, hemolysis study showed that the hemolysis ratio was less than 5% when the concentration of MM@BPPF was <800 μg/mL, demonstrating the superior biosafety of MM@BPPF during blood circulation (Fig. 2M)[53].

Overproduction of ROS, such as superoxide anions (O_2•$^-$) and hydrogen peroxide (H_2O_2), is a hallmark of oxidative stress and contributes to neuronal apoptosis and damage in IS. Therefore, scavenging excessive ROS is a potential strategy to alleviate I/R injury[54]. BP NSs exhibit unique redox properties due to the rapid electron transfer and P-O bond oxidative reaction induced by their layered structure (Fig. 2N). Therefore, BP NSs process catalase (CAT)-like activity and superoxide dismutase (SOD)-like activity through oxidizing H_2O_2 and consuming hydroxyl radicals (•OH) and O_2•$^-$[55]. In this context, the ROS scavenging ability of MM@BPPF was investigated using the widely adopted antioxidant activity assays including the 2,2-diphenyl-1-picrylhydrazyl radical (DPPH•) assay and the 2,2′-azino-bis (3-ethylbenzthiazoline-6-sulfonic acid) radical ion ($ABTS^{•+}$) assay[56]. As illustrated, the free-radical-scavenging ability of MM@BPPF was concentration-dependent, achieving ROS removal efficiencies of 82.92% in the DPPH• assay and 83.47% in the $ABTS^{•+}$ assay at BP NSs concentration of 125 μg/mL (Fig. 2O, P). Additionally, the •OH scavenging ability was determined by UV–vis spectroscopy at a wavelength of 510 nm. MM@BPPF exhibited strong •OH scavenging activity, removing approximately 90% of •OH at BP NSs concentration of 125 μg/mL (Fig. 2Q). Moreover, to explore the release profiles of PolyMet and FTY720 in mitochondria, MM@BPPF was dispersed in a pH 8.0 solution with or without 1.0 mM H_2O_2 to simulate the mitochondrial environment in normal cells and oxidatively stressed cells, respectively. As shown in Supplementary Fig. 4, only 4.8% and 4.17% of FTY720 and PolyMet were released from MM@BPPF in pH 8.0 solution without H_2O_2 at 2 h, whereas more than 81.34% of FTY720 and 66.74% of PolyMet were released at 2 h when exposure to 1.0 mM H_2O_2, respectively, indicating the strong ROS-responsive capacity of BP NSs that promoted nanocarrier degradation and allowed subsequent drug release. This markedly distinct drug release behavior between pH 8.0 condition with and without 1.0 mM H_2O_2 ensured the specific and rapid release of antioxidant within the mitochondria of oxidatively stressed cells following IS. Collectively, these results confirmed the potent antioxidant activity of MM@BPPF and highlighted its great potential for I/R injury treatment.

In vitro penetrability and targeting ability

In nose-to-brain delivery, the existence of physiological barriers in the nasal cavity limits the efficiency of drug delivery[32]. To monitor the permeability of MM@BPPF to the olfactory epithelium, a human nasal epithelial cell (HNEpC)-based cellular barrier model was established to mimic the transport of BP NSs and MM@BPPF in olfactory epithelium (Fig. 3A)[20]. Notably, both groups achieved effective permeability across the HNEpC monolayer, with MM@BPPF exhibiting a permeability rate of 77.00% and BP NSs showing a rate of 68.71% (Fig. 3B). Besides, to investigate the cellular binding interactions of this design, different formulations were labelled with Cy5 and the bEnd.3 cell membrane was tracked with DiO. Then, cells were treated with different formulations for 30 min and observed under confocal laser-scanning microcopy (CLSM). As shown in Fig. 3F, there was a clear co-localization of DiO and Cy5 fluorescence in cells treated with MM@BP-Cy5. In particular, this signal was stronger in MM@BP-Cy5-treated cells when compared to cells incubated with Mic@BP-Cy5 and Mit@BP-Cy5, suggesting an enhanced binding affinity of MM@BP-Cy5 to endothelial cells. Therefore, these findings indicated that MM@BPPF could effectively cross the nasal mucosal barrier. Next, the cellular uptake behavior of different formulations

https://doi.org/10.1038/s41467-025-68024-5

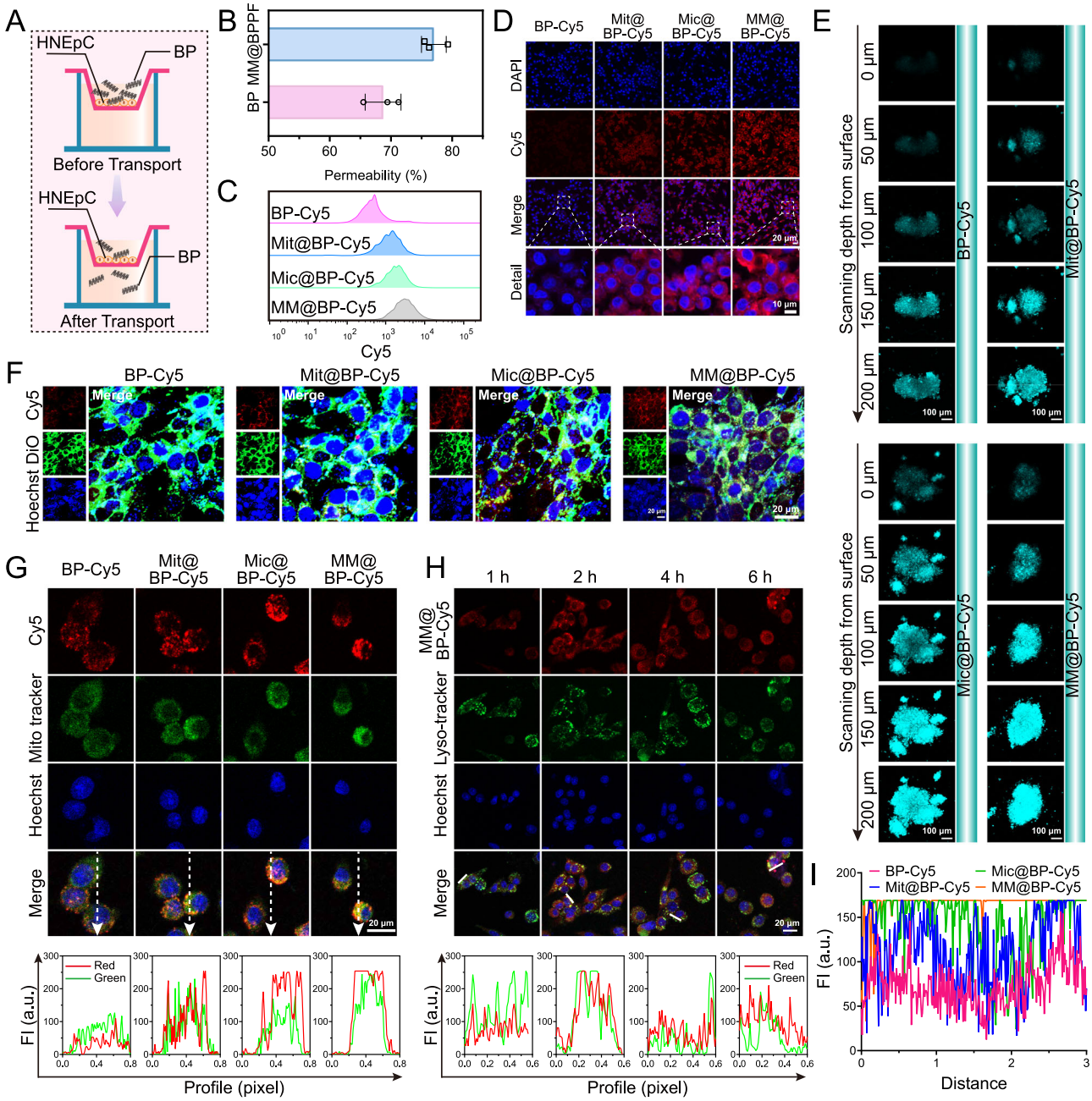

Fig. 3 | In vitro penetrability and targeting ability of MM@BPPF. A Schematic illustration of BP NSs and MM@BPPF transport across the HNEpC monolayer in the transwell model. **B** Quantitative analysis of the ability of BP NSs and MM@BPPF to cross the nasal mucosal barrier (The data represent the means ± SD, $n = 3$ independent experiments). **C** Flow cytometric quantification of PC12 cells subjected to OGD/R after incubation with BP-Cy5, Mic@BP-Cy5, Mit@BP-Cy5, and MM@BP-Cy5. **D** Cellular uptake behavior of various Cy5-labeled NPs in PC12 cells subjected to OGD/R, scale bar: 10 μm. The CLSM images were representative data from 3 independent experiments. **E** CLSM images scanned in Z-stack mode of 3D neurospheres treated with Cy5-labeled NPs, scale bar: 100 μm. The CLSM images were representative data from 3 independent experiments. **F** Binding interaction between DiO-stained bEnd.3 cells and Cy5-labeled NPs, scale bar: 20 μm. The CLSM images were representative data from 3 independent experiments. **G** Co-localization experiment of mitochondria and Cy5-labeled NPs in PC12 cells, scale bar: 20 μm. The CLSM images were representative data from 3 independent experiments. **H** Co-localization experiment of lysosome and MM@BP-Cy5 in PC12 cells, scale bar: 20 μm. The CLSM images were representative data from 3 independent experiments. **I** Fluorescence intensity of 3D neurospheres at the depth of 200 μm. Source data are provided as a Source Data file.

in oxygen and glucose deprivation/reoxygenation (OGD/R)-induced PC12 cells was analyzed using CLSM and flow cytometry (FCM). Apparently, cells treated with membrane-coated BP-Cy5 exhibited stronger Cy5 fluorescence than those treated with BP-Cy5, with MM@BP-Cy5-treated cells showing the highest fluorescence intensity, indicating the improved cellular internalization of prepared NPs (Fig. 3C, D). Consistently, FCM quantitative analysis corroborated these findings as well (Supplementary Fig. 5).

The poor penetration of drugs into the brain parenchyma, especially in ischemic-hypoxia areas after blood reperfusion, is one of the major challenges in the treatment of I/R injury[57]. Although MM@BP-Cy5 demonstrated superior nasal mucosal barrier permeability and efficient cellular uptake in OGD/R-induced PC12 cells, the penetration ability of various BP-based NPs was further evaluated in a 3D neurosphere model. Initially, 3D neurospheres were exposed to H_2O_2 treatment to mimic the oxidative stress conditions, followed by incubation

with different NPs for 2 h. Next, the penetration depth of Cy5-labeled NPs was examined by CLSM. Clearly, the fluorescence intensity of membrane-camouflaged NPs was significantly higher than that of BP-Cy5 at equivalent depths. Among the Mit@BP-Cy5, Mic@BP-Cy5, and MM@BP-Cy5 groups, MM@BP-Cy5-treated neurospheres displayed the strongest Cy5 fluorescence with the deepest penetration. CLSM images revealed that MM@BP-Cy5 fluorescence was extensively distributed throughout the 3D neurospheres, suggesting the inherent mobility of this bioengineered nanolamellar system and its strong penetration capability into the deep cerebral ischemic-hypoxic areas (Fig. 3E and I)[58,59]. This phenomenon could be explained by the innate chemotactic properties of MicM toward inflammatory regions and the subcellular homotypic targeting ability of MitM, collectively enabling MM@BP-Cy5 to achieve deep and efficient penetration within the 3D neurospheres.

At the early stage of reperfusion, the rapid increase in blood oxygen levels in the infract area triggered ROS release, leading to subsequent ischemic brain injury[60]. Mitochondria, as a kind of crucial organelle, provide almost 80% of cellular energy via oxidative phosphorylation and are considered to be a major source of ROS. Therefore, co-localization of NPs and mitochondria is essential for ROS scavenging and neuro-restoration. The in vitro mitochondrial targeting ability of different NPs was evaluated by tracking mitochondria (Mito tracker-labeled, green) and NPs (Cy5-labeled, red) in PC12 cells. As highlighted by CLSM images, Mit@BP-Cy5 and MM@BP-Cy5 were effectively taken up by PC12 cells and exhibited pronounced mitochondrial targeting, as evidenced by the perfect overlap of Mito tracker and Cy5 signals (Fig. 3G). In addition, lysosomes in PC12 cells were stained with commercial Lyso-tracker to examine the co-localization of MM@BP-Cy5. As the CLSM images suggested, red fluorescence from MM@BP-Cy5 was consistently observed in the cytoplasm. Notably, the overlap of red and green signals peaked at 2 h post-incubation and decreased by 6 h, indicating effective endocytosis followed by intracellular trafficking of MM@BP-Cy5 within PC12 cells (Fig. 3H). Since NPs can be engulfed by the mononuclear phagocyte system and cleared from the body, various kinds of cell membranes are extracted to cloak the NPs to facilitate immune evasion. Hence, the cellular uptake of NPs by RAW264.7 macrophage cells were analyzed using CLSM and FCM. A strong fluorescence signal was detected in BP-Cy5-treated cells, whereas the Cy5 signal was significantly diminished in cells treated with membrane-coated NPs, demonstrating the strong immune escape ability of biomimetic NPs (Supplementary Fig. 6). Overall, the above evidence indicated that MM@BP-Cy5 could effectively traverse the nasal mucosal barrier, target and penetrate PC12 cells exposed to OGD/R, and specifically accumulate in neuronal mitochondria.

In vitro therapeutic efficacy of MM@BPPF

First, an OGD/R model of PC12 cells was established in vitro to mimic I/R injury using the previously reported method[11]. Then, a series of experiments were designed to evaluate the neuroprotective effect of different NPs in cellular level. Cell viability following different treatments was initially assessed by MTT assay and live/dead staining assay. As indicated by CLSM images, OGD/R treatment induced the most apparent cell death with the brightest red fluorescence representing PI, confirming the successful establishment of the OGD/R model. After treatment with BP-based formulations, the signal of red fluorescence decreased significantly, while green fluorescence, indicating Calcein-AM markedly enhanced compared to the OGD/R group. Notably, almost all cells were rescued after MM@BPPF treatment (Fig. 4A). Meanwhile, MTT analysis revealed that BP NSs treatment increased the viability of PC12 cells to 50.07%. Moreover, BPF and BPPF treatments elevated PC12 cell viability to 64.31% and 76.45%, respectively, implying a synergistic effect between FTY720 and PolyMet. As expected, cells treated with MM@BPPF exhibited the highest viability and minimal cell damage (Fig. 4B). Afterward, the apoptosis of cells was determined by Annexin V/PI double staining assay and TUNEL staining. The apoptosis rate of MM@BPPF-treated cells dropped to 7.47%, which was much lower than that of the OGD/R treatment group (74.56%) (Fig. 4C, D). In addition, the intensity of the green TUNEL fluorescence was the weakest in MM@BPPF-treated cells (Fig. 4E). Therefore, FCM analysis and CLSM images consistently verified that MM@BPPF provided the most effective protection against cell apoptosis induced by OGD/R among all treatment groups. Overproduction of ROS is one of the major factors contributing to I/R injury after stroke attack, and the level of ROS is highly related to cell apoptosis[61,62]. Therefore, to evaluate the neuroprotective effect of the designed NPs, the intracellular ROS level in OGD/R-exposed PC12 cells was assessed using the DCFH-DA probe via CLSM and FCM analysis. As shown in Fig. 4F, a clear ROS signal was observed in PC12 cells subjected to OGD/R, indicating that the OGD/R condition dramatically increased ROS level and induced oxidative stress. Compared to the OGD/R condition, BP NSs, BPF, and BPPF treatments demonstrated notable ROS scavenging effects, as evidenced by a reduction in ROS intensity to varying degrees. In addition, FCM quantification confirmed that MM@BPPF exhibited the most effective ROS elimination capacity, suggesting its superior neuroprotective efficacy (Fig. 4G and Supplementary Fig. 7). Furthermore, given that lactate dehydrogenase (LDH) is rapidly released upon cell membrane damage, we measured LDH level to evaluate the cell membrane integrity[63]. Compared with the OGD/R group, LDH leakage was dramatically decreased after MM@BPPF treatment, returning to levels comparable to control group, indicating that MM@BPPF could effectively mitigate OGD/R-triggered cellular damage (Fig. 4I). Finally, cell migration ability after different treatments was assessed using wound healing assay. PC12 cells subjected to OGD/R showed negligible migration during the observation period, whereas MM@BPPF treatment significantly improved cell migration, which achieved a migration rate of 68.88% after 24 h, highlighting the superior neurorestorative function of MM@BPPF (Fig. 4H and Supplementary Fig. 8).

In vitro neuroprotective mechanisms of MM@BPPF

The findings above revealed that MM@BPPF could effectively localize to mitochondria and function as an antioxidant to reduce ROS levels in the OGD/R model. To further explore the mechanisms underlying MM@BPPF in regulating mitochondrial function, a series of experiments were investigated accordingly. To begin with, the morphonology of mitochondria in OGD/R-challenged PC12 cells after BP NSs and MM@BPPF treatments were observed by bio-TEM. According to the bio-TEM images, the mitochondria were severely swollen and disintegrated under OGD/R condition. However, BP NSs treatment apparently restored mitochondrial morphonology, indicating its favorable neuroprotective effects. Encouragingly, MM@BPPF displayed superior mitochondrial protection capability probably owing to the active targeting ability conferred by the MicM and MitM (Fig. 5A). In addition, excessive ROS can cause oxidative damage to mtDNA, leading to a decrease in mitochondrial membrane potential (MMP)[64]. Thus, MMP is considered as an indicator of mitochondrial activity. Inspired by the superior ROS scavenging ability of BP-based formulations, the MMP of cells after various treatments was detected by JC-1 probe[65]. According to CLSM images, BP NSs, BPF, BPPF, and MM@BPPF treatments significantly improved the MMP of PC12 cells, as evidenced by the increased red fluorescence and decreased green fluorescence (Fig. 5B). Quantitative analysis demonstrated that JC-1 aggregates in cells treated with BP NSs and MM@BPPF were significantly higher than those in OGD/R group (Supplementary Fig. 9). Besides, the MMP gradient generated by the electron transport chain can catalyze the synthesis of intracellular ATP, which is an important indicator of mitochondrial energy supply[66]. Therefore, we assessed the intracellular ATP levels in PC12 cells after treatments with different NPs using an ATP assay kit.

https://doi.org/10.1038/s41467-025-68024-5

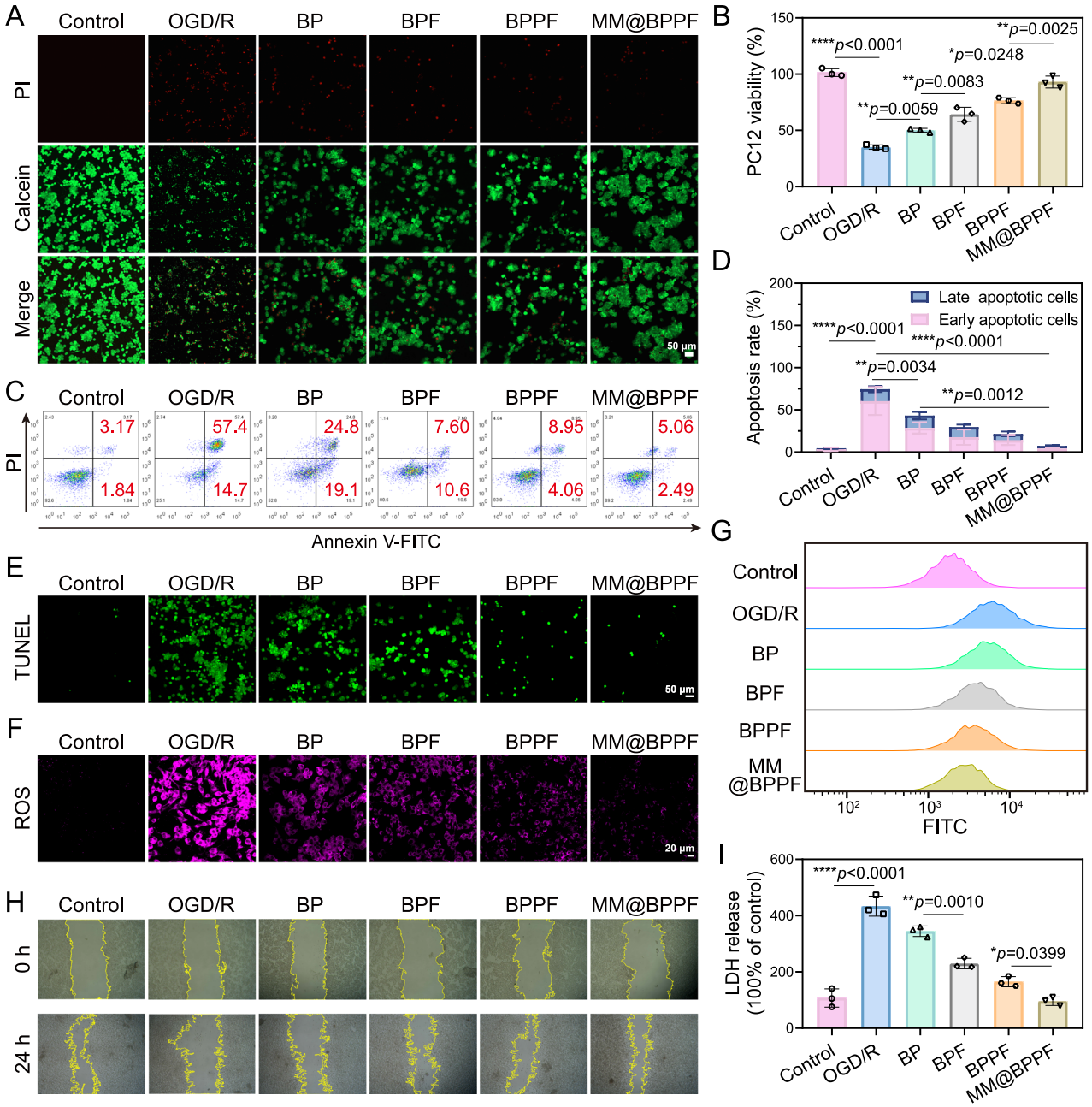

Fig. 4 | In vitro therapeutic efficacy of MM@BPPF. A Calcein-AM (live) and PI (dead) staining of PC12 cells subjected to OGD/R after different treatments. Normal PC12 cells were used as control, scale bar: 50 μm. **B** Cell viability of OGD/R-induced PC12 cells after different treatments by MTT assay. **C** FCM plots of Annexin V/PI-stained PC12 cells subjected to OGD/R after different treatments, and **D** their quantitative analysis. **E** TUNEL staining of PC12 cells subjected to OGD/R after different treatments, scale bar: 50 μm. The CLSM images were representative data from 3 independent experiments. **F** Detection of ROS levels in PC12 cells exposed to OGD/R after different treatments, scale bar: 20 μm, and **G** their flow cytometric quantification. The CLSM images were representative data from 3 independent experiments. **H** Wound healing assay of PC12 cells subjected to OGD/R after different treatments. The images were representative data from 3 independent experiments. **I** LDH levels in PC12 cells exposed to OGD/R after different treatments. The data represent the means ± SD, $n = 3$ independent experiments in (**B**, **D**, **I**). Statistics: one-way ANOVA with Tukey's multiple comparison test (**B**, **D**, **I**), $^{*}p < 0.05$, $^{**}p < 0.01$, $^{****}p < 0.0001$. Source data are provided as a Source Data file.

Apparently, oxidative stress induced by the OGD/R condition dramatically reduced ATP levels. Of note, treatment with BP NSs, BPF, and BPPF raised ATP levels by 1.39-, 1.98-, and 2.63-fold, respectively, compared to the OGD/R group. Noticeably, MM@BPPF treatment elevated ATP levels to the highest level, showing no significant difference in comparison to control group (Fig. 5F). Meanwhile, intracellular calcium levels were measured via FCM using Fluo-8 AM probe. As mitochondria and endoplasmic reticulum serve as major cellular calcium reservoirs, and their damage often results in significant calcium overload, which is a key consequence triggered by oxidative stress[67]. According to FCM assessment, the OGD/R condition significantly induced calcium overload, affecting 43.6% of the cells. In contrast, treatment with BP NSs, BPF, BPPF, and MM@BPPF reduced the percentage of calcium-overloaded cells to 13.69%, 11.99%, 7.56%, and 4.73%, respectively (Fig. 5C and G). Meanwhile, previous studies have reported that non-toxic PO_4^{3-}, a degradation production of BP NSs in physiological environment, is a critical component of biomineralization that can react with abundant free Ca^{2+}. Therefore, the

https://doi.org/10.1038/s41467-025-68024-5

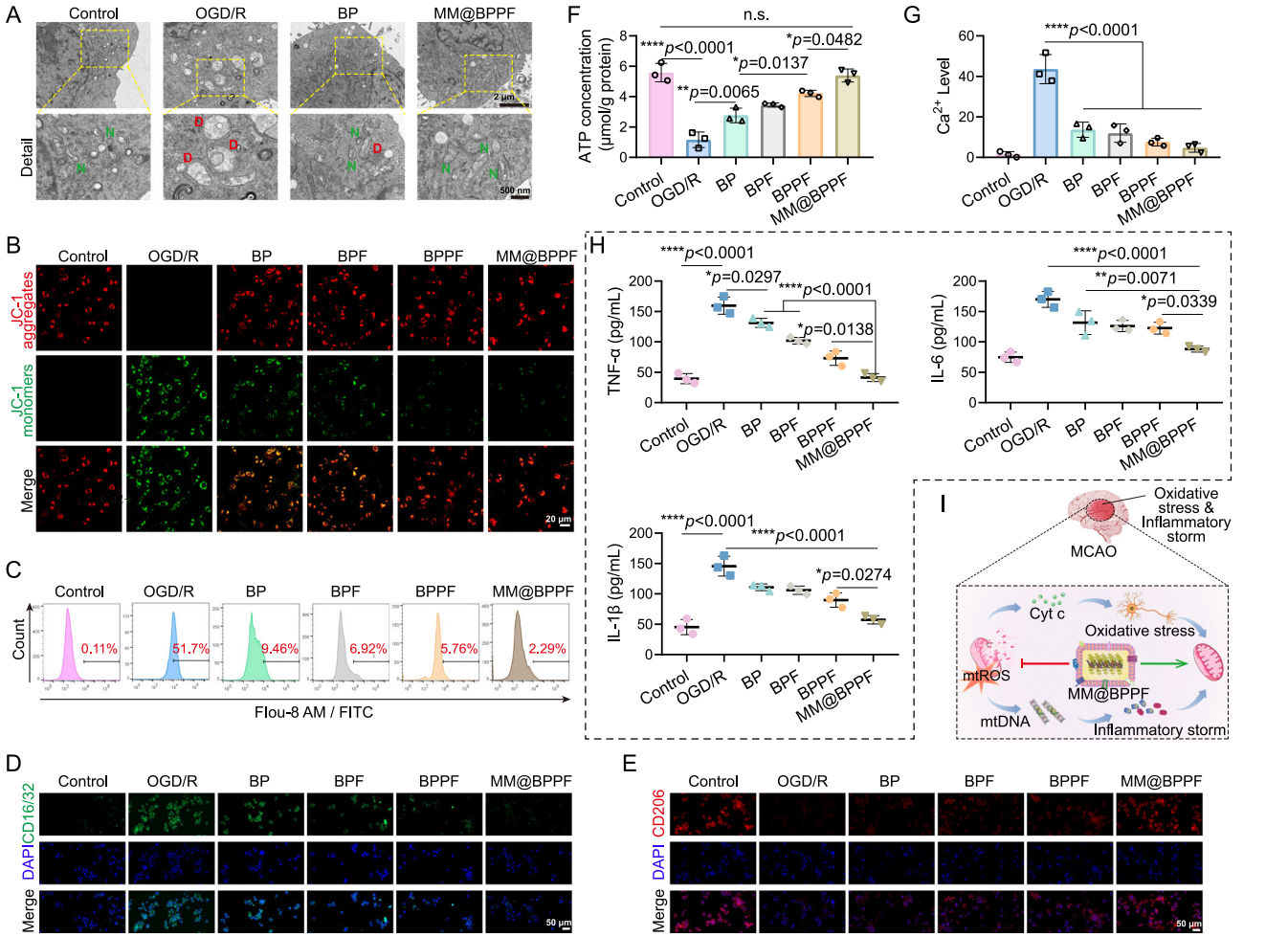

Fig. 5 | In vitro neuroprotective mechanisms of MM@BPPF. A Bio-TEM images of ODG/R-induced PC12 cells after different treatments, scale bar: upper: 2 μm, down: 500 nm. N normal, D damaged. The bio-TEM images were representative data from 3 independent experiments. **B** CLSM images of MMP detection in OGD/R-induced PC12 cells after different treatments. The CLSM images were representative data from 3 independent experiments. **C** Intracellular calcium detection in OGD/R model of PC12 cells after different treatments. **D** Immunofluorescence staining of CD16/32 (M1-like microglia marker), and **E** CD206 (M2-like microglia marker) in OGD/R-exposed BV2 cells after different treatments, scale bar: 50 μm. The immunofluorescence staining images were representative data from 3 independent experiments. **F** ATP concentration in PC12 cells exposed to OGD/R after different treatments. **G** Quantitative analysis of intracellular calcium levels in OGD/R model of PC12 cells after different treatments. **H** Pro-inflammatory cytokines levels in BV2 cells exposed to OGD/R after different treatments. **I** Schematic illustration of MM@BPPF inhibition of mtROS and regulation of mitochondrial function. The data represent the means ± SD, $n = 3$ independent experiments in (**F**–**H**). Statistics: one-way ANOVA with Tukey's multiple comparison test (**F**–**H**), $^{*}p < 0.05$, $^{**}p < 0.01$, $^{****}p < 0.0001$, n.s. no statistical significance. Source data are provided as a Source Data file.

interaction between PO_4^{3-} and Ca^{2+} could promote the removal of overloaded intracellular calcium, potentially indicating the effectiveness of MM@BPPF in maintaining mitochondrial function.

Among various cell types involved in intercellular crosstalk during IS and I/R injury (e.g., endothelial cells, perivascular neurons, microglia, etc.), microglia are the most sensitive to environmental stress and can be rapidly activated and recruited to ischemic regions immediately after stroke onset[68]. Therefore, we further evaluated the in vitro therapeutic effects of different formulations on microglia subjected to OGD/R. According to our findings, MM@BPPF significantly rescued OGD/R-induced BV2 cells, as evidenced by elevated cellular uptake, reduced cell apoptosis, increased ROS scavenging, and improved mitochondrial dysfunction (Supplementary Fig. 10). In addition, M1-like microglia release pro-inflammatory cytokines and promote oxidative stress during IS, facilitating neuronal injury and thus exacerbating neuroinflammation[69]. In contrast, M2-like microglia alleviate the inflammatory microenvironment and prevent neuronal injury by secreting anti-inflammatory cytokines. Thus, regulating microglial polarization represents a promising approach to prevent the deterioration caused by ischemic storke[70]. Moreover, ROS scavengers have been reported to polarize M1-like microglia into M2 type[71]. Therefore, an OGD/R model in BV2 cells was established to investigate the polarization effect of different formulations in vitro. The pro-inflammatory marker CD16/32 and the anti-inflammatory marker CD206 were stained by immunofluorescence to indicate microglial polarization after treatments with different BP-originated NPs. As revealed by CLSM images, OGD/R condition significantly increased the expression of CD16/32 marker on BV2 cells, suggesting a pro-inflammatory ischemic environment induced by oxidative stress. Concurrently, all treatments using BP-based NPs exerted anti-inflammatory capacity, as verified by the attenuated green fluorescence of CD16/32 and strengthened red fluorescence of CD206. Notably, MM@BPPF treatment caused the most effective BV2 polarization, illustrating the best microglial modulatory effects (Fig. 5D, E and Supplementary Fig. 11). Inspired by the outstanding microglial polarization capability of MM@BPPF, inflammatory cytokines secreted by OGD/R-induced BV2 cells after different treatments were detected by ELISA technology. As shown in Fig. 5H, BP-based formulations

markedly suppressed the secretion of pro-inflammatory cytokines such as TNF-α, IL-1β, and IL-6. Particularly, MM@BPPF treatment reduced the levels of these pro-inflammatory cytokines in BV2 cells to nearly those observed in normal cells. Altogether, these results indicated the favorable anti-inflammatory and neuroprotective effects of MM@BPPF in the context of acute IS (Fig. 5I).

In vivo brain distribution and mitochondria targeting ability

Intranasal administration has been recognized as an effective drug delivery approach to the brain due to improved brain distribution, decreased off-target distribution in major organs, and most importantly, the ability to bypass the BBB[32]. To determine the brain distribution of BP-based formulations after intranasal administration, we monitored the fluorescence signal in the brains of MCAO/R rats following intranasal administration of BP-Cy5, Mic@BP-Cy5, Mit@BP-Cy5, and MM@BP-Cy5. As Fig. 6A illustrated, the Cy5 signal could be observed in the nasal cavity in each group of MCAO/R rats. After 2 h of administration, Cy5 signal was detected in the brain regions of Mic@BP-Cy5, Mit@BP-Cy5, and MM@BP-Cy5-administered rats. These fluorescence signals reached their peaks at 4 h and then gradually declined during subsequent observation periods. In contrast, only weak fluorescence was observed in the brain after administration with naked NPs (BP-Cy5). Interestingly, Mic@BP-Cy5 presented more efficient brain delivery of therapeutics comparable to Mit@BP-Cy5, which might be attributed to the heightened sensitivity of microglia after acute IS. Notably, the in vivo fluorescence signal in the brain region of rats administered with MM@BP-Cy5 was sustained at a high level and was significantly stronger than that observed in other groups throughout the entire monitoring period, which was 4.27, 2.65, and 1.76 times as high as that of BP-Cy5, Mit@BP-Cy5, and Mic@BP-Cy5 groups, respectively, suggesting improved brain targeting efficiency (Fig. 6B). Subsequently, major organs were harvested from each rat at 24 h, and their brains were sectioned into five slices for imaging using the in vivo imaging system (IVIS). Quantitative fluorescence intensity of the brain tissues in MM@BP-Cy5 group was 11.09-fold, 4.67-fold, and 1.47-fold higher than that in BP-Cy5, Mit@BP-Cy5, Mic@BP-Cy5 groups at 24 h post-stroke, respectively, suggesting the preferential accumulation of MM@BPPF in brain regions (Supplementary Fig. 12A). Noteworthily, the functional modification of BP NSs by MitM and MicM enhanced their specific targeting ability to cerebral infarct regions, as evidenced by the prominent fluorescent signal distributed in the ischemic hemispheres (Fig. 6C). To further confirm the specific accumulation of MM@BP-Cy5 in ischemic hemisphere, brain tissues from MCAO/R rats administrated with different formulations was subjected to immunofluorescence staining of intercellular cell adhesion molecule-1 (ICAM-1). As Supplementary Fig. 12B illustrated, an evident green fluorescence signal was observed in the ischemic hemisphere, indicating that reperfusion significantly enhanced the expression of ICAM-1. Meanwhile, compared to normal hemisphere, NPs preferred to accumulate in ischemic hemisphere, as evidenced by the stronger red fluorescence. Besides, the intensity of red fluorescence representing MM@BP-Cy5 in ischemic brain was more apparent compared to bare BP-Cy5, indicating that MM had a strong affinity toward inflamed vascular endothelial cells. Therefore, these findings implicated that MM@BP-Cy5 possessed precise targeting ability to localize within the ischemic hemisphere. Additionally, we explored the in vivo brain entry pathway following intranasal administration by observing the distribution of MM@BP-Cy5 in the nasal cavity and along the trigeminal nerve. The images of nasal cavity clearly showed that Cy5 fluorescence distributed within the olfactory nerves across the sagittal plane, confirming the potential neuronal transport of MM@BPPF (Supplementary Fig. 13A). Moreover, as shown in Supplementary Fig. 13B, Cy5 fluorescence in the MM@BP-Cy5 group was clearly distributed across the trigeminal nerve, suggesting that MM@BP-Cy5 was effectively transported to the brain via the trigeminal nerve.

Subsequentially, we evaluated the cellular and subcellular targeting efficiency of MM@BP-Cy5. Firstly, the brain of MCAO/R rats after intranasal administration was sliced and the sections were co-stained with markers for neurons ($NeuN^+$) and microglia ($Iba\text{-}1^+$) to study the distribution of different formulations in these cells (Supplementary Fig. 14). The images of ischemic hemisphere showed that MM decoration markedly increased the overlap between the red fluorescence of Cy5 and the green fluorescence of neurons in comparison to bare BP group or single membrane coating group. Additionally, clear co-localization of Cy5 fluorescence was observed in small clusters within microglia. These results indicated that MM-decorated nanoplatform could effectively target both neurons and microglia within ischemic lesion. More importantly, the homologous membrane camouflage was anticipated to facilitate the accumulation of NPs in mitochondria. To verify this, brain tissues from each group were immunofluorescently stained with anti-hsp60 antibody, a key indicator of mitochondria, to validate the co-localization of NPs with mitochondria. Apparently, strong yellow fluorescence was observed in brain sections from MM@BP-Cy5-administered rats, indicating that MM-cloaked NPs exhibited superior mitochondrial co-localization efficiency (Fig. 6D). Collectively, the above results demonstrated that intranasal delivery of BP-based NPs after MM decoration not only enhanced their distribution in ischemic regions post-stroke, but also improved their accumulation in mitochondria, offering a promising therapeutic strategy in treating I/R injury based on mitochondrial function regulation (Fig. 6E).

Finally, to monitor the in vivo circulation time of different BP-based formulations, the fluorescence signal of plasma at various time points post-administration was evaluated via IVIS (Supplementary Fig. 15A). Both fluorescence images and quantitative analysis showed that BP-Cy5 was promptly eliminated from the blood circulation following intranasal administration. Comparatively, BP NSs modified with biomimetic membranes displayed noticeable fluorescence signals in blood samples collected at 12 h and 24 h, suggesting that membrane camouflage effectively prolonged the systemic circulation of the encapsulated cargos in vivo (Supplementary Fig. 15B).

In vivo therapeutic efficiency and neuroprotective effects

Building on the preferrable targeting capability of MM@BPPF, we further investigated its in vivo therapeutic and neuroprotective effects based on MCAO/R rat model as described previously[11]. First, we validated that nasal delivery represented as a superior approach compared to intravenous administration for the treatment of IS as discussed in detail in the Supplementary Results (Supplementary Fig. 16). Next, rats were randomly divided into six groups, including a sham-operated group and five treatment groups. Rats in treatment groups received intranasal administration of saline, BP NSs, BPF, BPPF, and MM@BPPF according to the predefined treatment schedule (Fig. 7A). Laser speckle imaging was firstly applied to directly visualize the focal cerebral blood flow (CBF) at different time points after different treatments. As shown in Fig. 7B, the CBF remained stable in the sham-operated group. However, the CBF declined dramatically after MCAO operation without remarkable recovery after saline treatment. Evidently, different BP-based treatments facilitated the restoration of bloodstream to varying degrees. Among them, MM@BPPF treatment led to the most rapid and pronounced therapeutic effect, restoring the CBF to a level nearly equivalent to that of sham-operated group after 24 h of reperfusion (Fig. 7D). Furthermore, the infarct volume was measured by triphenyl tetrazolium chloride (TTC) staining (Fig. 7C). Remarkably, MM@BPPF treatment markedly attenuated cerebral infarction, as evidenced by the extensive red TTC staining observed in their brain sections. Besides, quantitative analysis demonstrated that BP NSs treatment significantly alleviated I/R injury after IS attack, reducing the infarct volume from 38.19% in saline group to 23.63% (Fig. 7E). This therapeutic effect might be resulted from the

https://doi.org/10.1038/s41467-025-68024-5

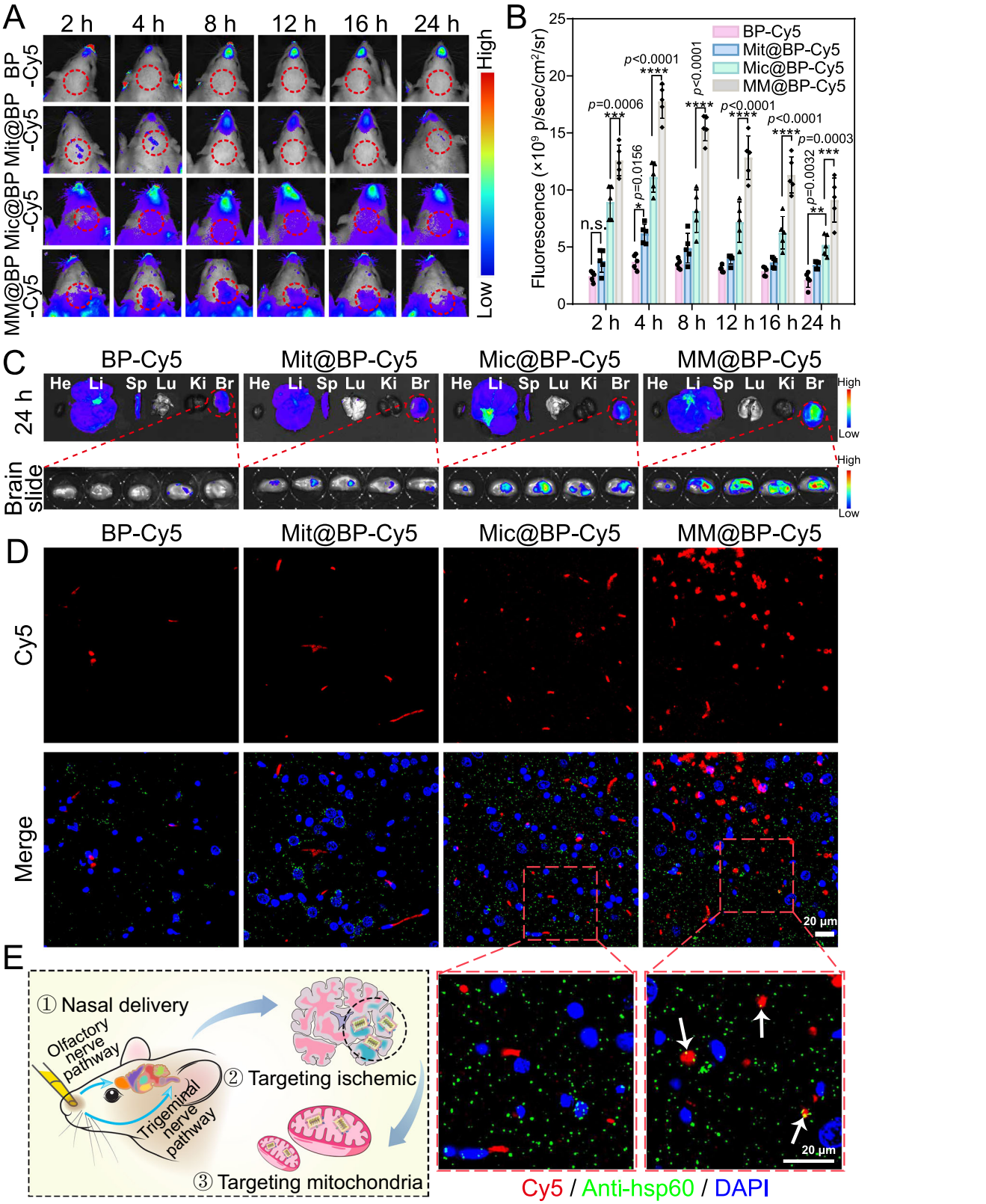

Fig. 6 | Evaluation of in vivo brain distribution and mitochondrial targeting ability of MM@BPPF. A In vivo imaging of the head of MCAO/R rats after different nasal administrations, and **B** their corresponding quantitative fluorescence intensity analysis (The data represent the means ± SD, $n = 5$ biological replicates. Statistics: one-way ANOVA with Tukey's multiple comparison test, $^{*}p < 0.05$, $^{**}p < 0.01$, $^{***}p < 0.001$, $^{****}p < 0.0001$, n.s. no statistical significance). **C** Ex vivo imaging of major organs and brain sections at 24 h post-nasal administration. He heart, Li liver, Sp spleen, Lu lung, Ki kidney, Br brain. **D** Fluorescence images of Cy5 distribution in IS regions and co-localization assay with mitochondria, scale bar: 20 μm. White arrow: co-localization of Cy5 and anti-hsp60. The fluorescence images were representative data from 5 rats. **E** Schematic illustration of the mitochondrial targeting ability of NPs after nasal administration. Source data are provided as a Source Data file.

https://doi.org/10.1038/s41467-025-68024-5

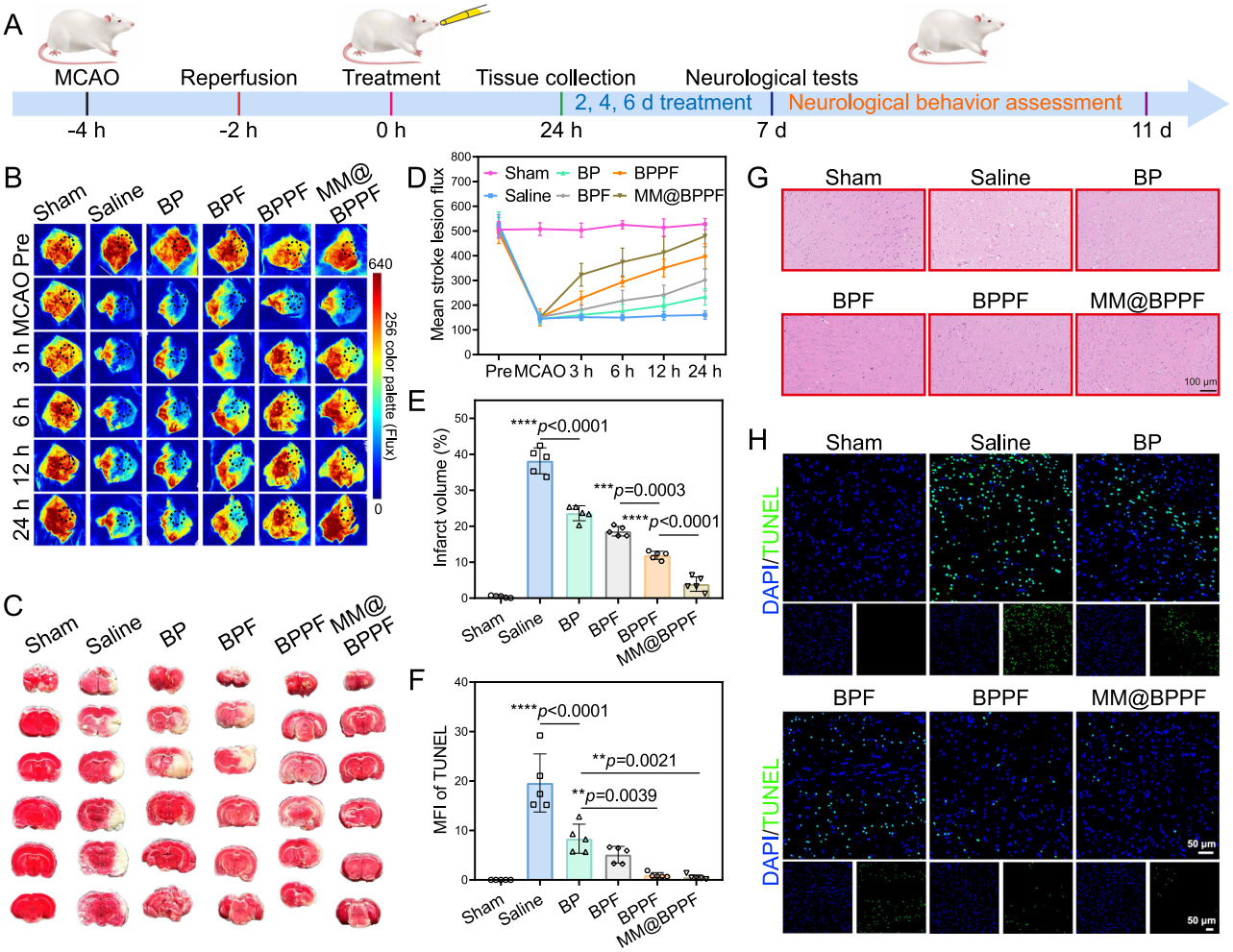

Fig. 7 | In vivo therapeutic efficiency after different treatments in MCAO/R rat model. A Treatment schedule of MCAO/R rats. **B** Laser speckle images of MCAO/R rats at different time points following intranasal administration of various NPs, and **D** their quantitative analysis. **C** TTC staining images of brain tissues harvested from different groups after different treatments. **E** Infarct volume measured by Image J software based on TTC staining images. **F** Mean fluorescence intensity of TUNEL after different treatments. **G** H&E-stained brain tissues of MCAO/R rats after different treatments, scale bar: 100 μm. The H&E staining images were representative data from 5 rats. **H** TUNEL-stained brain tissues of MCAO/R rats, scale bar: 50 μm. The TUNEL staining images were representative data from 5 rats. The data represent the means ± SD, $n = 5$ biological replicates in (**D**–**F**). Statistics: one-way ANOVA with Tukey's multiple comparison test (**E**, **F**), $^{**}p < 0.01$, $^{***}p < 0.001$, $^{****}p < 0.0001$. Source data are provided as a Source Data file.

antioxidant properties of BP NSs. Additionally, the further reduction in infarct volume following BPF and BPPF treatments highlighted the synergistic therapeutic effect of PolyMet and FTY720. Cerebral edema is a hallmark commonly associated with acute IS due to intravascular blockage and disruption of the BBB. To assess the extent of cerebral edema after different treatments, brain water content was measured by the dry-wet method. Obviously, saline-treated rats showed a significant increase in brain water content, reaching 88.86%, which was 1.23 times as high as those receiving MM@BPPF treatment (Supplementary Fig. 17). In addition, the survival rate of MCAO/R rats was prolonged during a two-week observation period in MM@BPPF group, suggesting its preferable therapeutic performance in mitigating I/R injury (Supplementary Fig. 18). Similar conclusions were drawn from H&E and TUNEL staining of brain sections. Specifically, H&E staining images revealed that compared to sham-operated group, saline-treated rats showed severe structural damage in their cerebral infarct area, which was characterized by neuron loss, tissue disorganization, and vacuolization (Fig. 7G). However, MM@BPPF treatment largely preserved the brain tissue architecture of rats suffered from MCAO/R, closely resembling that of normal brain tissue, thereby validating the potent therapeutic effectiveness of this designed bioengineered nanolamellar system in reversing the pathological alterations caused by cerebral IS. Meanwhile, the minimal green TUNEL fluorescence further confirmed the superior performance of MM@BPPF in preventing cell apoptosis and relieving neuronal injury (Fig. 7F and H). Collectively, all these findings demonstrated the potent therapeutic efficacy of intranasally administered MM@BPPF in the treatment of I/R-associated damage in vivo.

The antioxidant properties of BP-based NPs in infarct lesions were further investigated by detecting ROS level. As expected, MCAO/R operation triggered extensive cerebral ROS production, as indicated by the intense ROS signal. After different treatments with BP-based formulations, the ROS levels in brain decreased to varying extents (Fig. 8A). Significantly, after MM@BPPF treatment, ROS levels dropped to 11.28% of those observed in saline-administered group, implying the excellent ROS scavenging ability of this designed nanoplatform (Supplementary Fig. 19). Malondialdehyde (MDA) plays an important role in affecting the mitochondrial respiratory chain complex and regulating the activities of key enzymes within mitochondria, and the amount of MDA reflects the extent of cell membrane damage and cell death[72].

https://doi.org/10.1038/s41467-025-68024-5

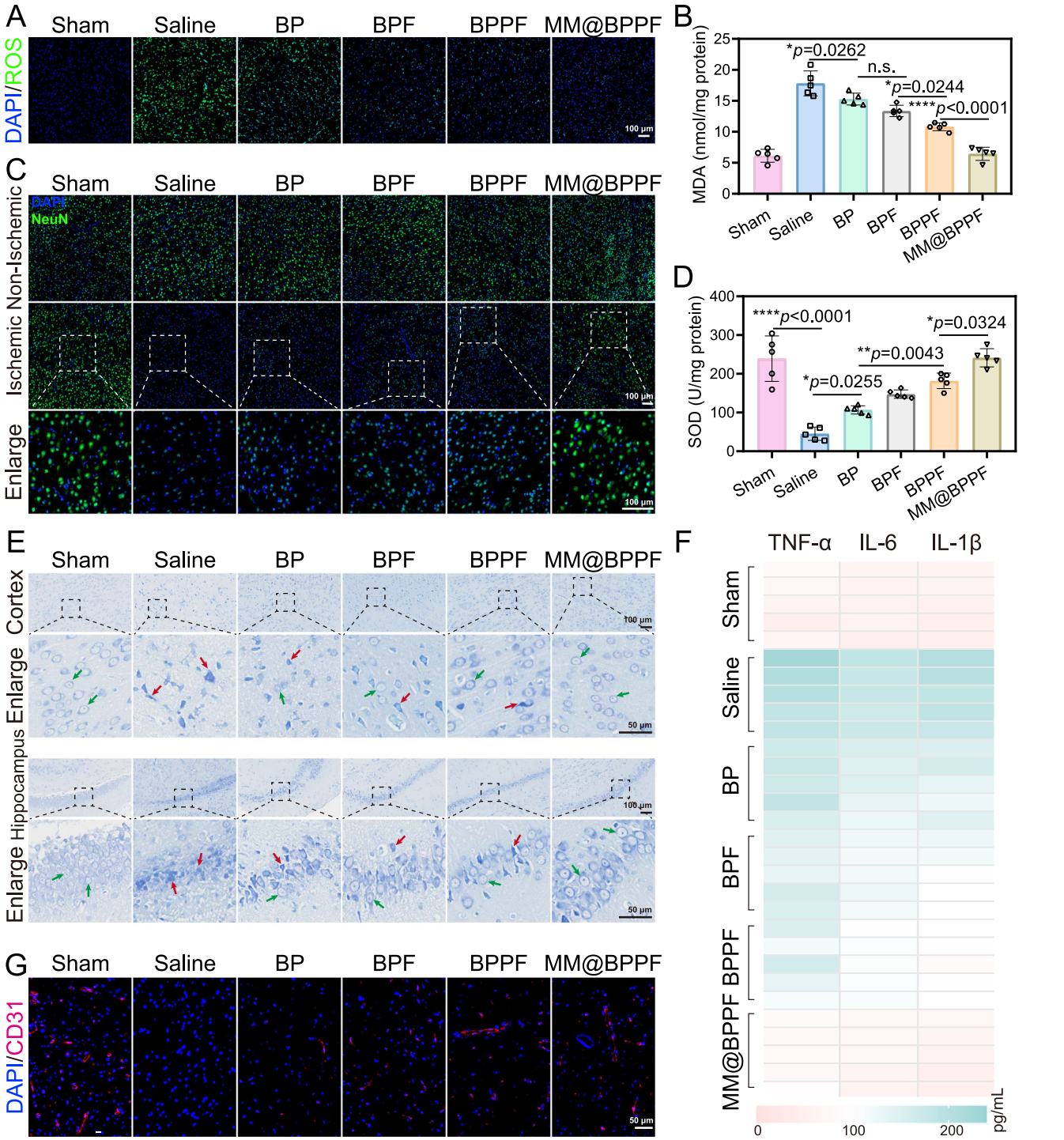

Fig. 8 | In vivo neuroprotective effects after different treatments in MCAO/R rat model. A ROS levels in ischemic brain lesions after different treatments, scale bar: 100 μm. **B** MDA content in ischemic brain lesions after different treatments. **C** NeuN immunofluorescence staining in non-ischemic and ischemic regions after different treatments, scale bar: 100 μm. **D** SOD content in ischemic brain lesions after different treatments. **E** Nissl staining of ischemic brain sections in cortex and hippocampus after different treatments, scale bar: upper: 100 μm, down: 50 μm. Green arrow: normal Nissl body. Red arrow: abnormal Nissl body. The Nissl staining images were representative data from 5 rats. **F** Heatmap of proinflammatory cytokine levels detected by ELISA in ischemic brain tissue after different treatments. **G** CD31 immunofluorescence staining in ischemic regions after different treatments, scale bar: 50 μm. The CD31 immunofluorescence staining images were representative data from 5 rats. The data represent the means ± SD, $n = 5$ biological replicates in (**B**, **D**). Statistics: one-way ANOVA with Tukey's multiple comparison test (**B**, **D**), $^{*}p < 0.05$, $^{**}p < 0.01$, $^{****}p < 0.0001$, n.s. no statistical significance. Source data are provided as a Source Data file.

Therefore, we measured MDA levels in MCAO/R rats to indirectly assess the oxidative damage in brain tissues. As depicted in Fig. 8B, treatments with BP-based formulations inhibited the production of MDA to varying degrees, among which, MM@BPPF treatment reduced the amount of MDA to the lowest level. Additionally, SOD is a crucial enzyme that protects mitochondria from oxidative damage and maintains normal mitochondrial functions by catalyzing ROS and lipid peroxides[73]. As demonstrated in Fig. 8D, SOD levels in brain of MCAO/R rats treated with MM@BPPF were significantly restored, signifying effective recovery of this key antioxidative enzyme in brain.

Collectively, these results confirmed that MM@BPPF could attenuate oxidative stress by scavenging free radicals, thus alleviating cellular damage. Next, the neuron-specific nuclear protein marker NeuN was stained to visualize neuronal apoptosis (Fig. 8C). Compared with saline treatment, almost 80% of neurons in ischemic area survived after MM@BPPF treatment (Supplementary Fig. 20A). Meanwhile, the percentages of surviving neurons in ischemic area increased progressively in BP NSs, BPF, and BPPF treatment groups, reaching 25.91%, 41.55%, and 54.90% of neurons, respectively. Notably, the number of surviving neurons in non-ischemic regions remained at the same level across all treatments, suggesting that MM@BPPF selectively targeted the cerebral ischemic lesions to regulate damaged neurons without exerting additional therapeutic effects on non-ischemic regions (Supplementary Fig. 20B). Next, brain sections from MCAO/R rats after different treatments were analyzed with Nissl staining to assess the functional status of neurons through evaluating the morphology and abundance of Nissl vehicles in the cortex and hippocampus (Fig. 8E). The results showed that the Nissl vehicles after sham operation and MM@BPPF treatment maintained a homogenous and intact vesicle shape, whereas a large number of Nissl vehicles were atrophied in saline group. Comparatively, the number of normal Nissl vehicles (green arrow) obviously increased after the intranasal application of different NPs, with MM@BPPF showing the most potent effect, which preserved over 91.88% of normal Nissl bodies in the cortex and 91.26% in the hippocampus, respectively. These findings demonstrated the effectiveness of designed nanolamellar system to alleviate neuronal necrosis and deformation in ischemic hemispheres (Supplementary Fig. 21). Previous studies have reported that BP NSs have a broad angiogenesis-promoting effect with significant therapeutic benefits in treating myocardial infarction and wound healing[74,75]. Moreover, metformin has also been reported to enhance angiogenesis in ischemic brain regions of MCAO/R rats[76]. Based on these facts, we investigated whether MM@BPPF retained this pro-angiogenic capability by performing CD31 immunofluorescence staining, which is a key indicator of nascent brain microvascular endothelia cells (Fig. 8G). Visually, CD31 expression was dramatically upregulated following BP NSs and BPPF treatments, suggesting the efficacy of BP NSs and PolyMet in promoting blood vessel regeneration. Consistently, quantification of the fluorescence intensity in the ischemic regions revealed a significant increase after BP NSs and BPPF treatments compared to saline group (Supplementary Fig. 22). Among various NPs, MM@BPPF showed the best performance in increasing cerebral vascular density, further confirming the precise targeting ability of this bioengineered nanolamellar system. Finally, ELISA was used to quantify the levels of pro-inflammatory factors in ischemic brain tissue after different treatments. Consistent with the in vitro results, the levels of TNF-α, IL-1β, and IL-6 were significantly increased after MCAO/R surgery, suggesting an inflammatory cytokine storm induced by MCAO/R. Notably, MM@BPPF treatment diminished the levels of these cytokines approaching to those of the sham-operated group, illustrating the potent effect of MM@BPPF in relieving neuroinflammation (Fig. 8F).

In vivo evaluation of neuroprotective mechanisms

To explore the in vivo neuroprotective mechanisms of prepared NPs, we first observed the morphology of mitochondria after different treatments using bio-TEM. As shown in Fig. 9A, after sham operation, mitochondria possessed normal morphology with a dense cristae structure without disintegration. In contrast, severe swelling with sparse cristae and vacuolization was clearly observed in the mitochondria distributed in the ischemic cerebral region of MCAO/R rats. Apparently, mitochondrial damage was reversed after BP NSs and MM@BPPF treatments, resulting in attenuated edema and well-preserved cristae structures, confirming the strong mitochondrial protective effect of MM@BPPF. In addition, we assessed the regulatory effect of different treatments on microglia polarization by immunofluorescence staining of Iba-1 (a general microglia marker), CD16/32 (a typical M1-like microglia marker), and CD206 (a typical M2-like microglia marker). As Fig. 9B, C illustrated, Iba-1 expression was significantly increased in saline group compared to sham-operated group, indicating the activation of microglia in response to I/R injury. Strikingly, BP-based treatments, particularly MM@BPPF, led to an apparent shift of microglia phenotype from M1-like into M2-like phenotype. The proportion of CD16/32-positive cells decreased to 17.99%, 9.42%, 5.35%, and 1.40% after BP NSs, BPF, BPPF, and MM@BPPF treatments, respectively (Fig. 9F). Conversely, the number of CD206-positive cells exhibited an increasing trend after different treatments, reaching 1.35, 1.54, 2.35, 7.32 times of that in saline group after BP NSs, BPF, BPPF, and MM@BPPF treatments, respectively (Fig. 9G). These results clearly demonstrated that both unmodified BP NSs and functionalized BP NSs could effectively promote microglial polarization from M1 phenotype to M2 phenotype, thereby exerting significant cerebroprotective effect. Furthermore, immunocyte infiltration in the ischemic hemisphere after different treatments was analyzed by FCM. $CD45^{high}$ peripheral monocytes/macrophages (Mo/MΦ) was identified by staining $CD11b^{+}$ myeloid cells with anti-CD45 antibody[77]. As shown in the FCM plots, the percentage of Mo/MΦ in cerebral brain tissue was prominently decreased after MM@BPPF treatment, suggesting that the neuroinflammation was dramatically alleviated using our designed treatment strategy (Fig. 9D and H). Similarly, macrophage, another important immunocyte related to neuronal injury, was also evaluated. In line with microglia, macrophages that accumulate in brain microenvironment can be categorized into two distinct types: one is pro-inflammatory phenotype, the other is anti-inflammatory phenotype[78]. M1-like macrophage aggravates brain inflammation by releasing pro-inflammatory factors, while M2-like macrophage mitigates brain injury by secreting anti-inflammatory cytokines. With the aim to evaluate the shifting of macrophage phenotype induced by our designed nanolamellar system, cerebral ischemic tissues after different treatments were analyzed by co-immunofluorescence staining of CD86 (M1-like macrophage marker) antibody and CD206 (M2-like macrophage marker) antibody using FCM[79]. As FCM results revealed, treatment with BP-based formulations markedly decreased the proportion of M1-like macrophage while increased the number of M2-like macrophage (Fig. 9E). The ratio of $CD206^{+}$ cells/$CD86^{+}$ cells increased from 0.15 in saline-treated group to 0.40, 0.60, 0.80, and 1.21 in BP NSs, BPF, BPPF, and MM@BPPF-treated groups, respectively (Fig. 9I). The gating strategies of immunocytes were presented in Supplementary Fig. 23. Taken together, these facts confirmed that MM@BPPF treatment effectively modulated the phenotypes of both microglia and macrophage, thereby reprogramming the inflammatory cerebral microenvironment and protecting neuronal cells from I/R injury.

In vivo evaluation of neurological function and biocompatibility

To assess the neurological and spatial cognitive function of MCAO/R rats after different treatments, the Morris water maze (MWM) test and the swimming trajectories of rats were recorded on day 11 (Fig. 10A). Evidently, rats receiving saline exhibited disorientation and erratic swimming patterns, confirming that MCAO/R surgery severely impaired their learning ability and spatial cognitive function. Encouragingly, rats treated with various NPs were able to successfully locate the submerged platform, demonstrating that their learning ability and spatial memory could be effectively rescued after performed treatments (Fig. 10B). Statistically, rats treated with MM@BPPF exhibited the shortest escape latency, which was 10.22 times shorter than those received saline treatment (Fig. 10C). Moreover, MM@BPPF-treated rats spent more time on the target quadrant after platform removal compared to saline-treated rats, with their path length being the longest among all treatment groups (Fig. 10D). In addition, saline-treated rats crossed the removed platform least frequently, while rats receiving MM@BPPF treatment

https://doi.org/10.1038/s41467-025-68024-5

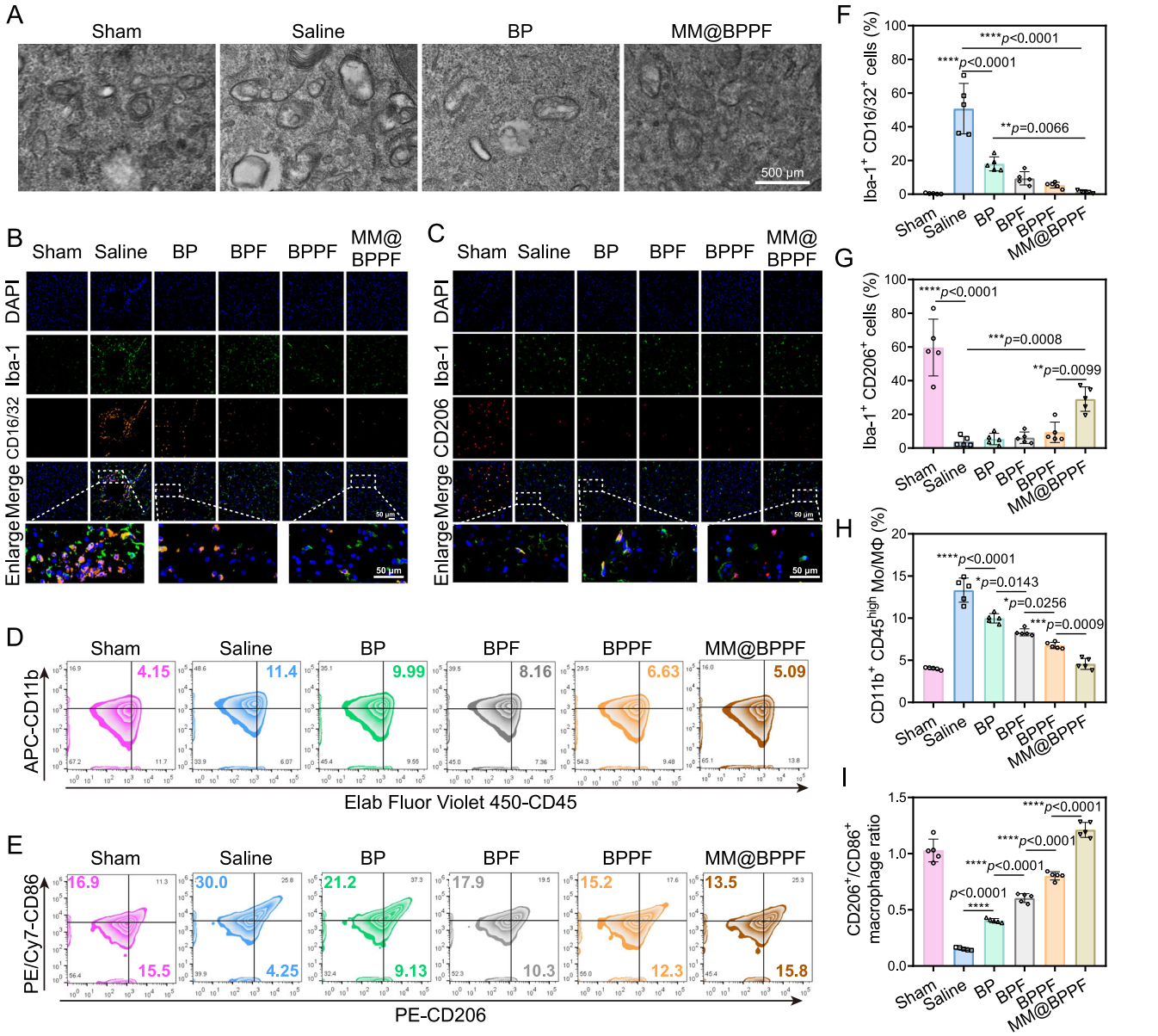

Fig. 9 | In vivo evaluation of neuroprotective mechanisms of MCAO/R rats after different treatments. A Bio-TEM images of mitochondria in IS regions of MCAO/R rats after different treatments, scale bar: 500 μm. The bio-TEM images were representative data from 5 rats. **B** Iba-1 and CD16/32 immunofluorescence staining to determine M1-like microglia levels in MCAO/R rats after different treatments, scale bar: 50 μm. The immunofluorescence staining images were representative data from 5 rats. **C** Iba-1 and CD206 immunofluorescence staining to determine M2-like microglia levels in MCAO/R rats after different treatments, scale bar: 50 μm. The immunofluorescence staining images were representative data from 5 rats. **D** FCM plots of Mo/MΦ in ischemic brain tissue of MCAO/R rats after different treatments. **E** FCM plots of M1-like macrophage and M2-like macrophage in ischemic brain tissue after different treatments. Quantitative analysis of **F** CD16/32 and **G** CD206 immunofluorescence levels in MCAO/R rats after different treatments. **H** Quantitative analysis of Mo/MΦ in ischemic brain tissue of MCAO/R rats after different treatments. **I** Quantitative analysis of the ratio of M2-like to M1-like macrophages in ischemic brain tissue after different treatments. The data represent the means ± SD, $n = 5$ biological replicates in (**F**–**I**). Statistics: one-way ANOVA with Tukey's multiple comparison test (**F**–**I**), $^{*}p < 0.05$, $^{**}p < 0.01$, $^{***}p < 0.001$, $^{****}p < 0.0001$. Source data are provided as a Source Data file.

crossed the platform more often (Fig. 10E). These findings verified that treatment with our designed nanoplatform could effectively restore the locomotor ability and cognitive functions of MCAO/R rats. Additionally, to further explore the long-term effects of different therapeutics on cognitive dysfunction in rats after IS attack, MWM test was also carried out 20 days after MCAO/R operation. Both learning and memory tests illustrated that rats receiving MM@BPPF treatment performed the best among all treatment groups (Supplementary Fig. 24). Finally, the behavior status of MCAO/R rats was assessed by the modified neurological severity score (mNSS), Bederson score, and Longa score (Fig. 10F and Supplementary Fig. 25). These neurological deficit scores were noticeably improved following treatment with various NPs compared to the saline group, suggesting that BP-based NPs played a vital role in the recovery of neurological and motor functions after I/R injury.

To evaluate the biosafety and biocompatibility of different formulations, saline, BP NSs, BPF, BPPF, and MM@BPPF were intranasally administered to healthy rats. First, open-field tests were performed to investigate whether different treatments affected the locomotor activity and anxiety-like behavior of the rodents. As shown in Fig. 10G–I, the running routes of the rats across different treatments were similar, with no significant difference in their total running

https://doi.org/10.1038/s41467-025-68024-5

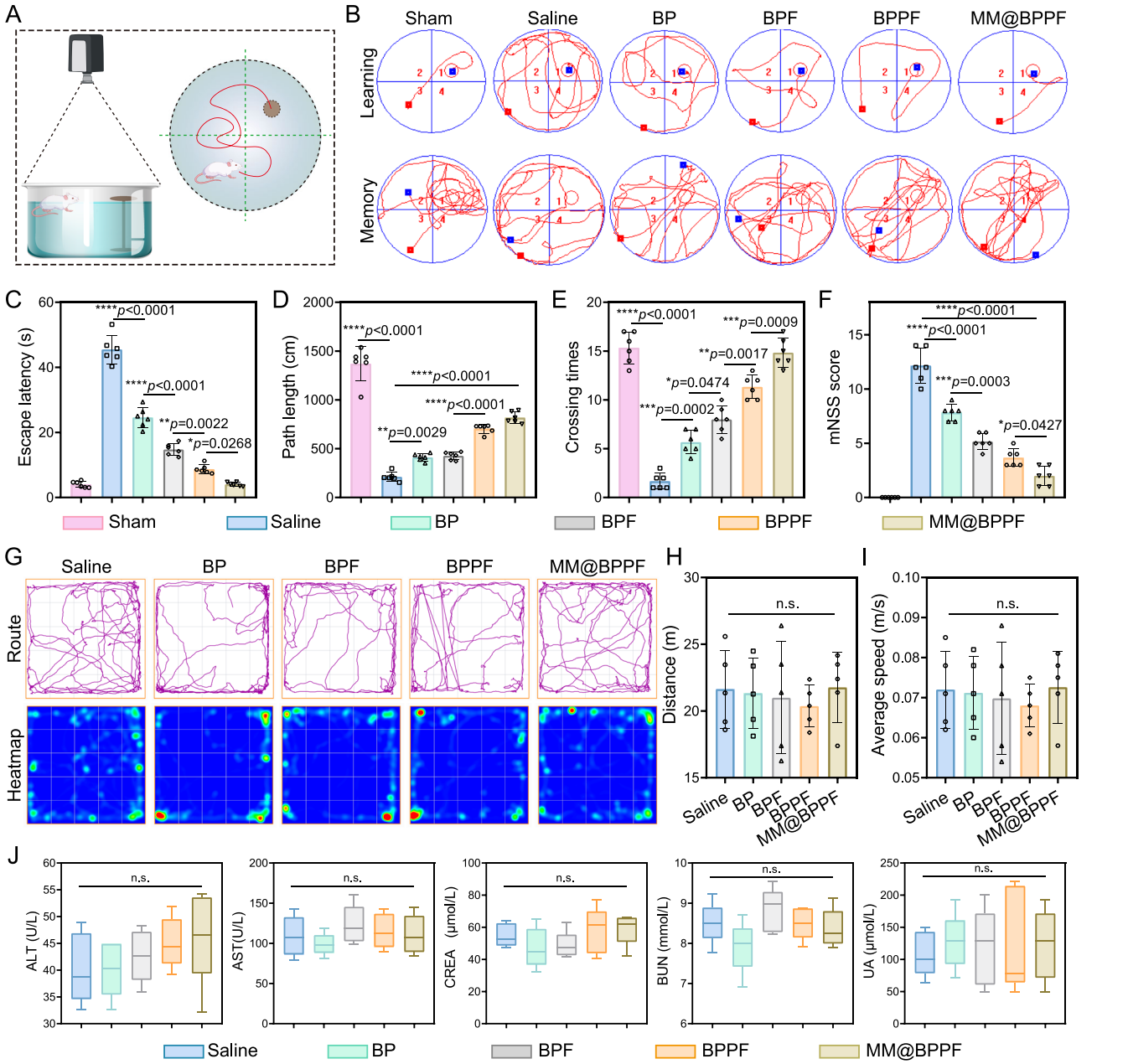

Fig. 10 | In vivo evaluation of neurological function and biocompatibility of rats after different treatments. A Schematic illustration of MWM test. **B** Respective swimming path of rats indicating their learning and memory ability by MWM test. **C** Escape latency of rats after different treatments 11 days after MCAO/R. **D** Path length at target quadrant of rats after different treatments 11 days after MCAO/R. **E** Crossing times of the removed platform of rats receiving different treatments 11 days after MCAO/R. **F** The mNSS score of rats receiving different treatments 11 days after MCAO/R. **G** Running routes and their heatmap of healthy rats after different treatments determined by open-field test. **H** Total distance, and **I** average speed of healthy rats after different treatments determined by open-field test. **J** Serum biochemical markers analysis of healthy rats after different treatments. Box plots show the median (center line), 25th to 75th percentiles (bounds of the box), and minimum to maximum values (whiskers). The data represent the means ± SD, $n = 6$ biological replicates in (**C**–**F**), $n = 5$ biological replicates in (**H**–**J**). Statistics: one-way ANOVA with Tukey's multiple comparison test (**C**–**F, H**–**J**), $^{*}p < 0.05$, $^{**}p < 0.01$, $^{***}p < 0.001$, $^{****}p < 0.0001$, n.s. no statistical significance. Source data are provided as a Source Data file.

distance and average speed. In addition, the serum biochemical markers of rats, including alanine aminotransferase (ALT), aspartate aminotransferase (AST), creatinine (CRE), uric acid (UA), and blood urea nitrogen (BUN), were performed to determine the blood compatibility of various NPs. According to the detected results, no significant difference was observed in these parameters (Fig. 10J). Moreover, major organs including heart, liver, spleen, lung, and kidney, were harvested for H&E staining. As illustrated, no obvious pathological alterations were observed in their main organs after different treatments (Supplementary Fig. 26). In conclusion, the above investigations confirmed that the designed bioengineered nanolamellar system exhibited desirable biosafety and biocompatibility in vivo.

Molecular mechanisms of MM@BPPF treatment

To further explore the molecular mechanisms underlying MM@BPPF treatment for I/R injury, whole genome RNA-sequencing was performed on the ischemic brain tissues from rats subjected to sham operation, or treated with saline, BP NSs, and MM@BPPF. As shown in Supplementary Fig. 27A, 1844 differentially expressed genes (DEGs) were detected between sham-operated and saline-treated groups

using VENN/UpSetR analysis, while the number of DEGs between MM@BPPF and saline groups increased to 4420, indicating that MM@BPPF treatment substantially modulated the expression of differential genes in ischemic brain tissue of MCAO/R rats. As shown by the volcano plots and histogram, 2402 detected genes (red dots) were upregulated, and 2018 detected genes (green dots) were downregulated in MM@BPPF group compared with saline group (Supplementary Fig. 27B, C). To further elucidate the relevant pathways involved in MM@BPPF treatment, the Kyoto Encyclopedia of Genes and Genomes (KEGG) analysis was performed to compare saline-treated group with the other treatment groups. As Supplementary Fig. 27D revealed, in comparison to sham-operated group, MCAO/R surgery enriched the DEGs associated with mitochondrial damage- and inflammation-related signaling pathways (red star), including NF-κB signaling pathway, TNF signaling pathway, TGF-β signaling pathway, and apoptosis pathway, indicating that mitochondrial damage and inflammatory responses were significantly activated following MCAO/R operation. Notably, MM@BPPF treatment enriched DEGs involved in the calcium signaling and VEGF signaling pathways, further confirming its potential to alleviate overloaded intracellular calcium and promote angiogenesis, which were consistent with the therapeutic effects observed both in vitro and in vivo (Supplementary Fig. 27E). Gene Ontology (GO) analysis revealed that MM@BPPF treatment mainly impacted on biological progress related to nervous system development, ion transport, neuron differentiation, and the positive regulation of neuron projection biological processes, as compared to saline treatment, implying that the neuroprotection effect could be effectively improved by our designed NPs (Supplementary Fig. 27F). Furthermore, the cluster heat map of genes associated with oxidative stress, mitochondrial function, inflammation, and apoptotic biological progressions verified that these biological processes were strongly modulated by MM@BPPF treatment in the context of IS (Supplementary Fig. 27G). Additionally, gene set enrichment analysis (GSEA) indicated that MM@BPPF treatment was closely associated with the activation of PPAR signaling pathway, which has been implicated to govern angiogenesis, apoptosis, and inflammation (Supplementary Fig. 27H)[80–82]. Besides, GSEA also revealed that MM@BPPF treatment might regulate ROS level through peroxisome-related pathway compared to saline treatment (Supplementary Fig. 27I)[83,84]. Collectively, these transcriptomic findings elucidated the molecular mechanisms underlying the neuroprotective effect of MM@BPPF and further supported its potential as a promising therapeutic strategy for IS management.

Discussion

In conclusion, we successfully designed and fabricated a bioengineered nanolamellar system derived from biomembrane-cloaked BP NSs, featuring mitochondrial targeting capability, potent antioxidant capacity, and microglial reprogramming potential for the treatment of cerebral I/R injury. This innovative design enabled efficient traversal of the nasal mucosal and deep penetration into brain tissue for effective neuronal internalization. Leveraging these features, MM@BPPF exhibited exceptional ROS scavenging ability, anti-inflammatory activity, and most importantly, the capacity to ameliorate mitochondrial dysfunction, as evidenced in vitro using OGD/R-exposed PC12 cells. Upon nasal administration, MM@BPPF treatment effectively targeted the cerebral ischemic brain tissues and further accumulated within the neuronal mitochondria of MCAO/R rats, thereby largely mitigating oxidative stress, attenuating neuronal damage, restoring mitochondrial function, alleviating inflammatory cascade, reprogramming microglial phenotypes, and promoting angiogenesis. As a result of these synergistic effects, MCAO/R rats treated with MM@BPPF showed improved spatial learning and memory performance, as along as with enhanced neurological scores, suggesting a successful rescue of ischemia-induced neurological deficits. Transcriptomic analysis further revealed that the neuroprotective mechanisms of MM@BPPF were closely linked to pathways involved in mitochondrial damage and inflammation. Overall, this study presents a potentially transformative therapeutic strategy by integrating BP-based formulations with biomimetic modification through intranasal delivery. This approach not only offers a powerful therapeutic option for cerebral I/R injury treatment through overcoming the challenges of BBB, but also holds great potential as a versatile nanoplatform for combating a broad range of CNS disorders.

Although the proposed strategy in this work presents distinctive advantages for I/R injury treatment, several limitations necessitate further investigation in the future. First, the therapeutic efficacy of intranasal administration has been significantly diminished by mucociliary clearance, enzymatic degradation in the respiratory epithelium, and the relatively limited area of olfactory epithelium compared to the entire nose mucosal surface area. These obstacles appeal the development of mucoadhesive delivery systems that improve adherence and tissue penetration. Secondly, the competition for spatial niches in the brain between peripheral immune cells and resident microglia warrants an investigation into the dynamic interactions between the CNS and infiltrating immune cells. Current study primarily focuses on the regulation of microglia polarization, while peripheral immune cells, such as neutrophils, macrophages, and lymphocytes, substantially affect the functional outcomes of IS by secreting inflammatory cytokines and producing neurotrophic factors and synaptic regulatory molecules around of the injured brain. Additional investigation into techniques that enhance dynamic interactions between immune cells and microglia demonstrates significant potential for improving post-stroke rehabilitation. Furthermore, the connections between the microglial subcluster and neural stem/precursor cells require persistent focus, as they constrain the neurogenic repair response following a stroke. Ultimately, the prevention of secondary stroke recurrence and associated injury still presents obstacles. Statistical analysis indicated that approximately 25% of first-time patients encountered a recurrent stroke within five years, resulting in significant secondary neurodegeneration. The current treatment strategy focuses mainly on improving outcomes post-stroke, whereas future research is expected to focus on preventing vascular reocclusion and minimizing stroke recurrence.

Methods

Ethical Statement

SD rats (250 × g ± 10 × g, male) were purchased from Huachuang Sino Biological Technology Co., Ltd. (Jiangsu, China) and housed at 24 ± 2 °C with 55 ± 5% humidity under normal 12 h light/dark cycle. All animal experiments were performed in compliance with National Institute of Health Guidelines for the Care and Use of Laboratory Animals and was approved by the Ethics Committee of China Pharmaceutical University (Ethics Code: 2024-10-004).

Materials

Bulk BP was purchased from Kunming Black Phosphorus Nanomaterial Technology Co., Ltd. (Kunming, China). Fingolimod (FTY720) hydrochloride was purchased from MedChemExpress (MCE) Co., Ltd. (Shanghai, China). Metformin hydrochloride and dicyandiamide were obtained from Sinopharm Chemical Reagent Co., Ltd. (Shanghai, China). Tris-magnesium buffer, 4′,6-diamidino-2-phenylindole (DAPI), Hoechst 33342, Calcein-AM/PI detection kit, Mito tracker, Lysosome tracker, JC-1 detection kit, and ATP assay kit were purchased from Beyotime Biotechnology Co., Ltd. (Shanghai, China). Annexin V-FITC/PI detection kit was purchased from Elabscience Co., Ltd. (Houston, USA). ROS detection kit was purchased from Biosharp Biotechnology Co., Ltd. (Beijing, China). The fluorescence-labelled antibodies used for immunocyte infiltrations: Elab Fluor® Violet 450 Anti-Mouse CD45

Antibody (Elabscience, E-AB-F1136Q, FC, not diluted); APC Anti-Mouse/Human CD11b Antibody (Elabscience, E-AB-F1081E, FC, not diluted); FITC Anti-Mouse F4/80 Antibody (Elabscience, E-AB-F0995C, FC, not diluted); PE/Cyanine7 Anti-Mouse CD86 Antibody (Elabscience, E-AB-F0994H, FC, not diluted); PE Anti-Mouse CD206/MMR Antibody (Elabscience, E-AB-F1135D, FC, not diluted).

Preparation of BP NSs and BPPF

BP NSs were obtained by a liquid exfoliation method as described previously[44]. Briefly, 15.0 mg bulk BP was dispersed in 15.0 mL acetone. Then, the dispersion was sonicated in an ice bath for 24 h and subsequently centrifuged at 1531 × *g* for 1 min. The supernatant was centrifuged at 16674 × *g* for 20 min, and the precipitate was washed three times with deoxygenated ultrapure water to remove acetone. Accordingly, the BP suspension was obtained.

BPPF was prepared by loading FTY720 and PolyMet onto BP NSs. Briefly, 1 mg BP NSs, 0.375 mg FTY720, and 0.375 mg PolyMet were dispersed in 5 mL deoxygenated ultrapure water and stirred at room temperature in the dark for 12 h. After centrifugation at 13780 × *g* for 15 min, the precipitate was washed three times with deoxygenated ultrapure water and then re-dispersed in water for further use.

Preparation of MM@BPPF

MM@BPPF were prepared according to the following producers. Firstly, MicM and MitM were prepared according to reported protocols[43,85]. Briefly, BV2 cells were resuspended in ice-cold Tris-magnesium buffer (pH 7.4, 0.01 M Tris containing 1 mM $MgCl_2$) at a concentration of 2.0×10^7 cells/mL and lysed overnight at 4 °C. These cells were then mixed with 1 M sucrose to a final concentration of 0.25 M. The suspension was further centrifuged at 2000 × *g*, 4 °C for 10 min. The supernatant was then collected and further centrifuged at 12,000 × *g*, 4 °C for 30 min. After two washes with ice-cold 0.25 M sucrose, MicM was obtained and stored at −80 °C for further use. MitM were obtained by first extracting the mitochondria using a mitochondrial extraction kit and then lysing the mitochondria. Specifically, PC12 cells were collected and resuspended in mitochondria extraction regent A containing PMSF (1 mM). After 15 min of incubation in an ice bath, the cells were disrupted by homogenization for 20 times in a glass homogenizer of appropriate size. Next, the mixture was centrifuged at 4 °C, 600 × *g* for 10 min. The supernatant was collected and further centrifuged at 4 °C, 11,000 × *g* for 10 min to collect mitochondria. The precipitate was resuspended with lysis buffer and then centrifuged at 4 °C, 100,000 × *g* for 70 min to obtain the MitM. The prepared MitM was lyophilized and stored at −80 °C for further use.

Secondly, MM@BPPF were prepared by co-extrusion of MM and BPPF[46]. The MicM solution was added equally to the MitM solution and then sonicated at 37 °C, 80 W for 5 min to obtain the MM. The MM solution and BPPF were then mixed and extruded using a liposome extruder (Avestin, Canada) to produce MM@BPPF.

Free-radical-scavenging capability of MM@BPPF

The free-radical-scavenging ability of MM@BPPF was determined by DPPH assay, ABTS assay, and •OH assay using UV–vis spectroscopy. Briefly, for the DPPH assay, 0.04 mg/mL of DPPH solution was mixed with 5.0 mL of different concentrations of MM@BPPF and then incubated for 30 min. Finally, the absorbance at 519 nm was measured by UV–vis spectroscopy.

For the ABTS assay, equal volumes of ABTS solution (7.4 mmol/L) and potassium persulfate solution (2.6 mmol/L) were mixed and allowed to react for 24 h in the dark to produce $ABTS^{\cdot+}$. The solution was then diluted 12 times with PBS buffer for further reaction with MM@BPPF. MM@BPPF solution and $ABTS^{\cdot+}$ solution was then mixed with equal volumes and incubated for 10 min. Finally, the absorbance at 734 nm was measured by UV–vis spectroscopy.

The •OH assay was performed according to the instructions of the •OH scavenging assay kit. The absorbance at 550 nm was measured to evaluate the amount of •OH.

Cell culture

Rat adrenal pheochromocytoma cell line PC12, murine macrophage cell line RAW264.7, murine microglia BV2 cells, and murine brain-derived endothelial cell line bEnd.3 were purchased from the Institute of Biochemistry and Cell Biology, Shanghai Institute of Biological Sciences, Chinese Academy of Sciences. Human nasal epithelial cells (HNEpC) were obtained from Procell (Wuhan, China). All of these cells were cultured in DMEM medium containing 10% fetal bovine serum (FBS) with 100 U/mL penicillin and 100 mg/mL streptomycin.

Transport of MM@BPPF through a HNEpC cell monolayer

The permeability of BP NSs and MM@BPPF was determined according to the published method[20]. Firstly, HNEpC cells were seeded in the upper chamber at a density of $5 \times 10^5/cm^2$ to establish a monolayer. Subsequently, 0.3 mL DMEM containing BP NSs or MM@BPPF was added to the donor side and 1.0 mL DMEM medium was added to the recipient side. After 2 h incubation, the upper chamber solution was collected and the concentration of BP NSs was determined using a UV–vis spectrometer. The permeability of BP NSs and MM@BPPF was then calculated using the following equation:

$$\text{Permeability}\ (\%) = \frac{C_0 - C_S}{C_0} \times 100\%$$

where c_0 and c_s refer to the initial and post-incubation concentrations of BP NSs and MM@BPPF, respectively.

Mitochondria and lysosome colocalization assay

PC12 cells subjected to OGD/R were seeded in confocal dishes and incubated with BP-Cy5, MitM@BP-Cy5, MicM@BP-Cy5, and MM@BP-Cy5 for 6 h. The cells were washed with PBS and stained with Mito Tracker at 37 °C. The nucleus was then stained with Hoechst 33342 for 10 min. Then, the staining solution was replaced with fresh medium. Finally, the cells were visualized under the CLSM. For lysosome co-localization analysis, the cells incubated with MM@BP-Cy5 for different time periods were stained with Lysosome Tracker. The distribution of NPs, mitochondria, and lysosomes was analyzed using Image J software.

Permeation ability in 3D cellular spheroids

3D cellular spheroids of PC12 cells were prepared using the previous method with modifications[57]. First, 60 μL low melting point agarose (1%) was added into 96-well plate and cooled and solidified at room temperature. Then, 1.0×10^3 PC12 cells were added into each well. The cells were cultured for 3 days to form 3D cellular spheroids. The medium was replaced every day. Afterward, FBS-free DMEM medium containing different formulations with H_2O_2 were added into each well and incubated for 2 h. After washing with PBS, the spheroids were placed on confocal dishes and scanned by the CLSM.

In vitro neuroprotective effects

The evaluation of cellular neuroprotective effects was performed in the OGD/R model by using PC12 cells and BV2 cells. After OGD/R for 4 h, the cells were cultured with different formulations for 24 h. The treated cells were then incubated with ROS probe (DCFH-DA) and TUNEL probe to further determine the level of cellular ROS and degree of cell apoptosis. For calcium detection, the cells were harvested and stained with Fluo-8 AM, followed by FCM for quantitative analysis.

Detection of mitochondrial function

First, the structure of mitochondria was observed by bio-TEM. Briefly, PC12 cells subjected to the OGD/R model were treated with different formulations for 24 h. The cells were then washed three times with PBS and pre-fixed with 2.5% glutaraldehyde for 5 min at room temperature. The cells were then collected using a cell scraper. The mixture was centrifuged at 106 × *g* for 3 min. Next, the supernatant was removed and replaced with fresh 2.5% glutaraldehyde to fix the cells for 30 min at room temperature. Finally, the samples were stored at 4 °C and subjected to bio-TEM detection. To detect MMP, PC12 subjected to the OGD/R model were seeded in confocal dishes and treated with different formulations for 24 h. The cells were then incubated with JC-1 solution at 37 °C for 20 min. Afterward, the cells were washed with JC-1 buffer. Finally, the cells were observed under the CLSM. The ATP level after different treatments was determined according to the instructions of the ATP assay kit.

Establishment of MCAO/R rat model

A MCAO/R model was established by using male rats according to published protocol[3]. Briefly, rats were anaesthetized during the experimental periods. Then, the right common carotid artery (CCA), external carotid artery (ECA), and internal carotid artery (ICA) of the rats were exposed and isolated. Next, the blood flow to the CCA was occluded with a slipknot, and the ECA was cut with a small incision at the distal end. The blood flow from the right middle cerebral artery was then blocked by carefully inserting the silicon-coated nylon monofilament (0.26 mm in diameter) into the ICA. After 120 min of occlusion, the silicon-coated nylon monofilament was removed to achieve reperfusion. Rats in the sham-operated group received the same procedures as above except for occlusion.

Therapeutic efficacy in the MCAO/R rat model

MCAO/R rats were randomly divided into sham-operated, saline, BP NSs, BPF, BPPF, and MM@BPPF groups. After 2 h of reperfusion, 20 μL of differently prepared formulations were administered intranasally to the rats under anesthesia. CBF was measured at different times using a Full Field Laser Perfusion Imager (SIM BFI-ZOOM Pro, Simopto, China). Then, the rats in each group were sacrificed. The brains from these rats were sectioned for TTC staining, H&E staining, TUNEL staining, immunofluorescence staining, immunohistochemical staining, and bio-TEM observation[86].

In vivo immunocyte infiltrations

Ischemic brain tissues from MCAO/R rats after different treatments were harvested and prepared for single cell suspensions. The cells were then washed with PBS and centrifuged at 231 × *g* for 5 min at 4 °C, followed by cell lysis with red blood cell lysis buffer. Next, the cells were collected and counted at a density of 1×10^6 cells. The sample from each group was resuspended with 200 μL PBS and stained with the corresponding antibodies for 20 min. Finally, the stained cells were collected, resuspended, and detected by FCM.

Neurological behavior assessment

To assess the neurological impairment, the learning and memory abilities of MCAO/R rats after different treatments were evaluated using the MWM test. Briefly, the rats were placed in a circular pool 200 cm in diameter and 50 cm in height filled with water at 25 ± 1 °C. For the learning phase from day 7 to day 11, a platform was placed in the first quadrant and the rats were put into the pool from the third quadrant. The time and distance the rats took to reach the platform were recorded. For the memory ability test, the platform in the first quadrant was removed and the swimming path and times of rats to cross the platform were recorded.

RNA sequencing

Brain tissue was collected and sent to Huada Company (BGI Genomics, Shenzhen, China) for RNA extraction and sequencing, and Dr. Tom Multi-omics Data mining system (https://biosys.bgi.com) was used for the following analysis and data mining.

Statistical analysis

All the experimental data was analyzed as mean ± S.D. The data were analyzed through One-Way ANOVA with a Tukey's test in multiple groups, and the statistical significance was expressed as $^*p < 0.05$, $^{**}p < 0.01$, $^{***}p < 0.001$, $^{****}p < 0.0001$, n.s. no statistical significance. All data were analyzed with GraphPad 8.0 software.

Reporting summary

Further information on research design is available in the Nature Portfolio Reporting Summary linked to this article.

Data availability

The authors declare that the data supporting of this study are presented in the article and Supplementary information files. Source data are provided with this paper. Sequence data that support the findings of this study have been deposited in NCBI Sequence Read Archive (SRA) with the BioProject accession: PRJNA1279262. Source data are provided with this paper.

References

1. Martin, S. S. et al. 2024 heart disease and stroke statistics: a report of US and global data from the American Heart Association. *Circulation* **149**, e347–e913 (2024).
2. Powers, W. J. Acute ischemic stroke. *N. Engl. J. Med.* **383**, 252–260 (2020).
3. Iadecola, C. & Anrather, J. The immunology of stroke: from mechanisms to translation. *Nat. Med.* **17**, 796–808 (2011).
4. Phipps, M. S. & Cronin, C. A. Management of acute ischemic stroke. *BMJ* **368**, l6983 (2020).
5. Tang, L. et al. Combining nanotechnology with the multifunctional roles of neutrophils against cancer and inflammatory disease. *Nanoscale* **14**, 1621–1645 (2022).
6. Li, S. et al. Artificial mesenchymal stem cell extracellular vesicles enhanced ischemic stroke treatment through targeted remodeling brain microvascular endothelial cells. *Acta Pharm. Sin. B* **15**, 4248–4264 (2025).
7. Wu, S. et al. Mesenchymal stem cells with polydopamine-coated NaGdF4 nanoparticles with Ca2+ chelation ability for ischemic stroke therapy. *Adv. Mater.* **37**, e2416020 (2025).
8. Wang, S. et al. Inhibiting mitochondrial damage for efficient treatment of cerebral ischemia-reperfusion injury through sequential targeting nanomedicine of neuronal mitochondria in affected brain tissue. *Adv. Mater.* **36**, e2409529 (2024).
9. Hu, X. et al. Microglial and macrophage polarization-new prospects for brain repair. *Nat. Rev. Neurol.* **11**, 56–64 (2015).
10. Eltzschig, H. K. & Eckle, T. Ischemia and reperfusion-from mechanism to translation. *Nat. Med.* **17**, 1391–1401 (2011).
11. Tang, L. et al. Blood-brain barrier-penetrating and lesion-targeting nanoplatforms inspired by the pathophysiological features for synergistic ischemic stroke therapy. *Adv. Mater.* **36**, e2312897 (2024).
12. Wu, D. et al. Pathogenesis-adaptive polydopamine nanosystem for sequential therapy of ischemic stroke. *Nat. Commun.* **14**, 7147 (2023).
13. He, M. et al. Black phosphorus nanosheets protect neurons by degrading aggregative alpha-syn and clearing ROS in Parkinson's disease. *Adv. Mater.* **36**, e2404576 (2024).

14. Yin, Y. et al. Microneedle patch-involved local therapy synergized with immune checkpoint inhibitor for pre- and post-operative cancer treatment. *J. Control. Release* **379**, 678–695 (2025).
15. He, Z. et al. Resolvin D1 delivery to lesional macrophages using antioxidative black phosphorus nanosheets for atherosclerosis treatment. *Nat. Nanotechnol.* **19**, 1386–1398 (2024).
16. Hou, J. et al. Treating acute kidney injury with antioxidative black phosphorus nanosheets. *Nano Lett.* **20**, 1447–1454 (2020).
17. Bigham, A. et al. Black phosphorus-based nanoplatforms for cancer therapy: chemistry, design, biological and therapeutic behaviors. *Chem. Soc. Rev.* **54**, 827–897 (2025).
18. Liu, H. et al. Black phosphorus, an emerging versatile nanoplatform for cancer immunotherapy. *Pharmaceutics* **13**, 1344 (2021).
19. Ma, Z., Zeng, P., Zhai, T., Zhao, Y. & Liang, H. In situ mitochondrial biomineralization for drug-free cancer therapy. *Adv. Mater.* **36**, e2310218 (2024).
20. Liu, Y. et al. Customized intranasal hydrogel delivering methylene blue ameliorates cognitive dysfunction against Alzheimer's disease. *Adv. Mater.* **36**, e2307081 (2024).
21. Jiang, S. et al. AMPK: potential therapeutic target for ischemic stroke. *Theranostics* **8**, 4535–4551 (2018).
22. Tang, L. et al. Leveraging nano-engineered mesenchymal stem cells for intramedullary spinal cord tumor treatment. *Chin. Chem. Lett.* **34**, 107801 (2023).
23. Tang, L. et al. Chemoimmunotherapeutic nanogel for pre- and postsurgical treatment of malignant melanoma by reprogramming tumor-associated macrophages. *Nano Lett.* **24**, 1717–1728 (2024).
24. Cao, Y. et al. Black phosphorus quantum dot loaded bioinspired nanoplatform synergized with aPD-L1 for multimode cancer immunotherapy. *Nano Lett.* **24**, 6767–6777 (2024).
25. Tang, L. et al. Extracellular vesicles-derived hybrid nanoplatforms for amplified CD47 blockade-based cancer immunotherapy. *Adv. Mater.* **35**, e2303835 (2023).
26. Zhao, Y. et al. Neutrophil membrane-camouflaged polyprodrug nanomedicine for inflammation suppression in ischemic stroke therapy. *Adv. Mater.* **36**, e2311803 (2024).
27. Liu, J. et al. The potential capacities of FTY720: novel therapeutic functions, targets, and mechanisms against diseases. *Eur. J. Med. Chem.* **290**, 117508 (2025).
28. Muñoz, J. P. et al. FTY720-P, a biased S1PR ligand, increases mitochondrial function through STAT3 activation in cardiac cells. *Int. J. Mol. Sci.* **24**, 7374 (2023).
29. Wang, X. et al. Drug delivery pathways to the central nervous system via the brain glymphatic system circumventing the blood-brain barrier. *Exploration* **5**, 20240036 (2024).
30. Guo, L. S. et al. Exploring the diagnostic potential: magnetic particle imaging for brain diseases. *Mil. Med. Res.* **12**, 18 (2025).
31. Lv, W. et al. Advances of nano drug delivery system for the theranostics of ischemic stroke. *J. Nanobiotechnology* **20**, 248 (2022).
32. Wang, G. et al. Tailored borneol-modified lipid nanoparticles nasal spray for enhanced nose-to-brain delivery to central nervous system diseases. *ACS Nano* **18**, 23684–23701 (2024).
33. Hu, J. et al. Intranasal delivery of near-infrared and magnetic dual-response nanospheres to rapidly produce antidepressant-like and cognitive enhancement effects. *Adv. Mater.* **36**, e2405547 (2024).
34. Shen, X. et al. Exploring the potential to enhance drug distribution in the brain subregion via intranasal delivery of nanoemulsion in combination with borneol as a guider. *Asian J. Pharm. Sci.* **18**, 100778 (2023).
35. Deruyver, L., Rigaut, C., Lambert, P., Haut, B. & Goole, J. The importance of pre-formulation studies and of 3D-printed nasal casts in the success of a pharmaceutical product intended for nose-to-brain delivery. *Adv. Drug Deliv. Rev.* **175**, 113826 (2021).
36. Kang, Y. et al. Nanocarrier-based transdermal drug delivery systems for dermatological therapy. *Pharmaceutics* **16**, 1384 (2024).
37. Chen, L. et al. Recent progress in targeted delivery vectors based on biomimetic nanoparticles. *Signal Transduct. Target. Ther.* **6**, 225 (2021).
38. Wu, J. et al. Nanotechnology reinforced neutrophil-based therapeutic strategies for inflammatory diseases therapy. *Nano Today* **46**, 101577 (2022).
39. Su, J. et al. Visualization of nasal powder distribution using biomimetic human nasal cavity model. *Acta Pharm. Sin. B* **14**, 392–404 (2024).
40. Tang, L. et al. Size-switchable and dual-targeting nanomedicine for cancer chemoimmunotherapy by potentiating deep tumor penetration and antitumor immunity. *Chem. Eng. J.* **493**, 152590 (2024).
41. Liao, J. et al. Magnetic field driven ceria nanosystems for mitochondria targeted therapy of ischemic stroke. *Adv. Funct. Mater.* **35**, 2423291 (2025).
42. He, W. et al. Drug-free biomimetic oxygen supply nanovehicle promotes ischemia-reperfusion therapy in stroke. *Adv. Funct. Mater.* **33**, 2212919 (2023).
43. Zou, Y. et al. Cancer cell-mitochondria hybrid membrane coated Gboxin loaded nanomedicines for glioblastoma treatment. *Nat. Commun.* **14**, 4557 (2023).
44. Xiao, Q. et al. Two-pronged attack: dual activation of fat reduction using near-infrared-responsive nanosandwich for targeted anti-obesity treatment. *Adv. Sci.* **11**, e2406985 (2024).
45. Wang, Y. et al. Synergistic therapy for cervical cancer by codelivery of cisplatin and JQ1 inhibiting Plk1-mutant Trp53 axis. *Nano Lett.* **21**, 2412–2421 (2021).
46. Liu, H. et al. Photoresponsive multirole nanoweapon camouflaged by hybrid cell membrane vesicles for efficient antibacterial therapy of *Pseudomonas aeruginosa*-infected pneumonia and wound. *Adv. Sci.* **11**, e2403101 (2024).
47. Su, Y. et al. A neutrophil membrane-functionalized black phosphorus riding inflammatory signal for positive feedback and multimode cancer therapy. *Mater. Horiz.* **7**, 574–585 (2020).
48. Cheng, G. et al. Swiss Army Knife" black phosphorus-based nanodelivery platform for synergistic antiparkinsonian therapy via remodeling the brain microenvironment. *J. Control. Release* **353**, 752–766 (2023).
49. Zhao, Y. et al. PolyMetformin combines carrier and anticancer activities for in vivo siRNA delivery. *Nat. Commun.* **7**, 11822 (2016).
50. Mei, Y. et al. A minimally designed PD-L1-targeted nanocomposite for positive feedback-based multimodal cancer therapy. *Mater. Today* **60**, 52–68 (2022).
51. Yin, Y. et al. Targeted microglial membrane-coated microRNA nanosponge mediates inhibition of glioblastoma. *ACS Nano* **18**, 29089–29105 (2024).
52. Fan, Q. et al. Multiple synergistic effects of the microglia membrane-bionic nanoplatform on mediate tumor microenvironment remodeling to amplify glioblastoma immunotherapy. *ACS Nano* **18**, 14469–14486 (2024).
53. Gao, J. et al. A nano-strategy for advanced triple-negative breast cancer therapy by regulating intratumoral microbiota. *Nano Lett.* **25**, 6134–6144 (2025).
54. Du, Y. et al. Ultrasmall iron-gallic acid coordination polymer nanodots with antioxidative neuroprotection for PET/MR imaging-guided ischemia stroke therapy. *Exploration* **3**, 20220041 (2023).
55. Lu, H. et al. Radical-scavenging and subchondral bone-regenerating nanomedicine for osteoarthritis treatment. *ACS Nano* **17**, 6131–6146 (2023).
56. Mei, Y. et al. Versatile hydrogel-based drug delivery platform for multimodal cancer therapy from bench to bedside. *Appl. Mater. Today* **39**, 102341 (2024).
57. Wang, R. et al. Biomimetic nanomotors for deep ischemia penetration and ferroptosis inhibition in neuroprotective therapy of ischemic stroke. *Adv. Mater.* **37**, e2409176 (2025).

58. Shi, J. et al. Bioinspired nanosponge for salvaging ischemic stroke via free radical scavenging and self-adapted oxygen regulating. *Nano Lett.* **20**, 780–789 (2019).
59. Tang, L. et al. Micro/nano system-mediated local treatment in conjunction with immune checkpoint inhibitor against advanced-stage malignant melanoma. *Chem. Eng. J.* **497**, 154499 (2024).
60. Liao, J. et al. Bioactive ceria nanoenzymes target mitochondria in reperfusion injury to treat ischemic stroke. *ACS Nano* **18**, 5510–5529 (2024).
61. Kong, J., Chu, R. & Wang, Y. Neuroprotective treatments for ischemic stroke: opportunities for nanotechnology. *Adv. Funct. Mater.* **32**, 2209405 (2022).
62. Ding, X. et al. Enhanced blood-brain barrier penetrability of BACE1 SiRNA-loaded prussian blue nanocomplexes for Alzheimer's disease synergy therapy. *Exploration* **5**, e20230178 (2025).
63. Oka, N. et al. Protective effects of alpha-mangostin encapsulated in cyclodextrin-nanoparticle on cerebral ischemia. *J. Control. Release* **353**, 216–228 (2023).
64. Tang, L. et al. Dual-targeting nanozyme combined with aPD-L1-based immunotherapy for combating cancer recurrence and metastasis. *Mater. Today* **73**, 79–95 (2024).
65. Tang, L. et al. Bioorthogonal chemistry-guided inhalable nanoprodrug to circumvent cisplatin resistance in orthotopic nonsmall cell lung cancer. *ACS Nano* **18**, 32103–32117 (2024).
66. Giacomello, M., Pyakurel, A., Glytsou, C. & Scorrano, L. The cell biology of mitochondrial membrane dynamics. *Nat. Rev. Mol. Cell Biol.* **21**, 204–224 (2020).
67. Huang, G. et al. Bioactive nanoenzyme reverses oxidative damage and endoplasmic reticulum stress in neurons under ischemic stroke. *ACS Nano* **16**, 431–452 (2022).
68. Gosselin, D. et al. An environment-dependent transcriptional network specifies human microglia identity. *Science* **356**, eaal3222 (2017).
69. Tang, L. et al. Harnessing nanobiotechnology for cerebral ischemic stroke management. *Biomater. Sci.* **11**, 791–812 (2023).
70. Liu, Y. et al. MLIF modulates microglia polarization in ischemic stroke by targeting eEF1A1. *Front Pharm.* **12**, 725268 (2021).
71. Zeng, F. et al. Custom-made ceria nanoparticles show a neuroprotective effect by modulating phenotypic polarization of the microglia. *Angew. Chem. Int. Ed. Engl.* **57**, 5808–5812 (2018).
72. Wei, L. et al. Multifunctional PHC bandage for accelerated wound healing in movable parts. *Exploration* **5**, 20230176 (2025).
73. Zhang, Y. et al. Biomimetic design of mitochondria-targeted hybrid nanozymes as superoxide scavengers. *Adv. Mater.* **33**, e2006570 (2021).
74. Bai, X. et al. Two-dimensional biodegradable black phosphorus nanosheets promote large full-thickness wound healing through in situ regeneration therapy. *ACS Nano* **18**, 3553–3574 (2024).
75. Zhang, J. et al. Targeted delivery of black phosphorus nanosheets by ROS responsive complex hydrogel based on angiogenesis and antioxidant promotes myocardial infarction repair. *J. Nanobiotechnology* **22**, 433 (2024).
76. Jin, Q. et al. Improvement of functional recovery by chronic metformin treatment is associated with enhanced alternative activation of microglia/macrophages and increased angiogenesis and neurogenesis following experimental stroke. *Brain Behav. Immun.* **40**, 131–142 (2014).
77. Liu, Q. et al. Peripheral TREM1 responses to brain and intestinal immunogens amplify stroke severity. *Nat. Immunol.* **20**, 1023–1034 (2019).
78. Becher, B., Spath, S. & Goverman, J. Cytokine networks in neuroinflammation. *Nat. Rev. Immunol.* **17**, 49–59 (2016).
79. Fu, C. et al. Bacterial outer membrane vesicles-clothed nanoparticles delivered by live macrophages for potentiating antitumor photoimmunotherapy. *Chem. Eng. J.* **499**, 156420 (2024).
80. Hiukka, A., Maranghi, M., Matikainen, N. & Taskinen, M. R. PPARalpha: an emerging therapeutic target in diabetic microvascular damage. *Nat. Rev. Endocrinol.* **6**, 454–463 (2010).
81. Bougarne, N. et al. Molecular actions of PPARalpha in lipid metabolism and inflammation. *Endocr. Rev.* **39**, 760–802 (2018).
82. Straus, D. S. & Glass, C. K. Anti-inflammatory actions of PPAR ligands: new insights on cellular and molecular mechanisms. *Trends Immunol.* **28**, 551–558 (2007).
83. Zhang, J. et al. ATM functions at the peroxisome to induce pexophagy in response to ROS. *Nat. Cell Biol.* **17**, 1259–1269 (2015).
84. He, A., Dean, J. M. & Lodhi, I. J. Peroxisomes as cellular adaptors to metabolic and environmental stress. *Trends Cell Biol.* **31**, 656–670 (2021).
85. Su, Y. et al. Macrophage membrane-camouflaged lipoprotein nanoparticles for effective obesity treatment based on a sustainable self-reinforcement strategy. *Acta Biomater.* **152**, 519–531 (2022).
86. Sun, S. et al. Smart liposomal nanocarrier enhanced the treatment of ischemic stroke through neutrophil extracellular traps and cyclic guanosine monophosphate-adenosine monophosphate synthase-stimulator of interferon genes (cGAS-STING) pathway inhibition of ischemic penumbra. *ACS Nano* **17**, 17845–17857 (2023).

Acknowledgements

This work was funded by the National Nature Science Foundation of China (no. 82573579 to W.W., 32071387 to W.W., and 31872756 to W.W.), Six Talent Peaks Project in Jiangsu Province (JY-079 to W.W.). L.T. acknowledges the Alexander von Humboldt Foundation for financial support, D.L. is partly supported by a grant from the Alzheimer's Association (24AARFD-1192360).

Author contributions

W.W., Y.Y., L.T., and D.L. conceived and designed the project. Y.Y., Z.L., W.S., H.L., Zihan W., C.F., Yuanbo Z., X.L., Yi Z., B.L., Zixuan W., and Q.Z. performed the experiments. Y.Y., L.T., D.L., Z.L., W.S., and Zihan W. analyzed the data. Y.Y. and L.T. wrote the manuscript. L.T., W.W., Y.Y., and D.L. reviewed and edited the manuscript. W.W. and L.T. supervised the entire project. W.W., L.T., and D.L. provided suggestions. All authors discussed the results and commented on the manuscript.

Competing interests

The authors declare no competing interests.

Additional information

Supplementary information The online version contains supplementary material available at https://doi.org/10.1038/s41467-025-68024-5.

Correspondence and requests for materials should be addressed to Dan Liu, Lu Tang or Wei Wang.

Peer review information *Nature Communications* thanks Bingyang Shi and the other, anonymous, reviewer(s) for their contribution to the peer review of this work. A peer review file is available.